



3D Numerical Assessment of Rammed Aggregate Pier Performance under Dynamic Loading in Liquefiable Soils

Georgios Zalachoris, Ph.D.¹; Dimitrios Zekkos, Ph.D., P.E., M.ASCE²; Alba Yerro, Ph.D., M.ASCE³; G. Allen Bowers, Ph.D., P.E., M.ASCE⁴; and Kord J. Wissmann, Ph.D., P.E., D.GE, M.ASCE⁵

Abstract: Ground improvement (GI) techniques have shown promise in effective liquefaction mitigation, but the physical mechanisms governing their three-dimensional (3D) response during dynamic loading are not yet fully understood. To evaluate the 3D performance of one GI technique, the rammed aggregate pier (RAP), in-situ site characterization, full-scale field test data, and calibrated baseline constitutive soil model parameters are combined to model the 3D fully coupled hydromechanical response of natural (unreinforced) and improved (reinforced) soil profiles. To the authors' knowledge, this contribution represents the first 3D model of a columnar-reinforced soil profile being calibrated using full-scale field testing. The field observations from the comprehensive ground improvement testing (GIT) program in New Zealand and insights from two-dimensional (2D) finite-difference analyses using constitutive model parameters calibrated against the field measurements were used. The developed 3D models were subjected to dynamic loads simulating the excitation generated by a vibroseis truck at one of the in-situ test sites of the GIT program, as well as unidirectional and bidirectional earthquake ground motions from the Canterbury Earthquake Sequence events. The 3D simulations showed that the improved soil profiles experienced reduced excess pore pressures and reduced dynamically induced shear strains compared to the natural, unreinforced soil models. The developed 3D finite-element predictions were compared and validated vis-à-vis the field observations of the GIT program. Compared to 2D analyses, 3D analyses provide a more accurate description of actual field conditions, and, for instance, it was observed that multidirectional shaking has a significant effect on liquefaction triggering, particularly for natural soil profiles. Finally, it was shown that soil densification around the installed pier elements and the lateral earth pressure increase within the densified soil and are the primary ground improvement mechanisms contributing to the reduction of dynamically induced shear deformations and excess pore pressure generation during earthquake shaking. It was also found that the permeability and shear stiffness of the installed RAP piers did not have a significant influence on the pore pressure response and shear strains developed along the centerline of the improved area. DOI: [10.1061/JGGEFK.GTENG-10795](https://doi.org/10.1061/JGGEFK.GTENG-10795). © 2023 American Society of Civil Engineers.

Introduction

During the last decades, large earthquake events (e.g., 1964 Niigata, Japan; 1995 Kobe, Japan) have resulted in extensive soil liquefaction with severe consequences on the built environment. More recently, much of the nearly NZ\$40 billion infrastructure damage following the 2010–2011 Canterbury Earthquake Sequence (CES) in Christchurch, New Zealand, was caused by extreme levels of liquefaction-induced deformations of structures with shallow foundations (Cubrinovski et al. 2011). Consequently, throughout the last two decades, the geotechnical engineering

community has allocated significant resources to theoretical and experimental research efforts focused on better understanding the physical mechanisms of the observed liquefaction-related phenomena, as well as on determining alternatives for the mitigation of liquefaction-induced damage (e.g., Seed et al. 2003; Idriss and Boulanger 2008; Wissmann et al. 2015; Roberts 2017; Green et al. 2018; Hutabarat and Bray 2021).

In engineering practice, structures built in areas characterized by the presence of liquefiable soils are commonly founded on deep foundation systems. To avoid the additional costs typically associated with deep foundation systems, an effective alternative has been the ground improvement of the soils near the ground surface (Ishihara 1985; Dimitriadi et al. 2017; Green et al. 2018). These ground improvement techniques increase the liquefaction resistance of soils by inducing soil densification, accelerating drainage, and increasing the overall stiffness of the soil (Green et al. 2008; Green and Lee 2012). Techniques such as deep dynamic compaction and vibrocompaction have traditionally been employed to densify liquefiable soils, and some of the more recent ground improvement methodologies include rapid impact compaction (RIC), low-mobility grout (LMG), and stone columns. Although the effectiveness of the more traditional ground improvement methods is well documented, the efficacy of columnar-reinforced soil profiles has not been comprehensively assessed. There are many different stone column construction techniques, and the construction details affect their performance. One of the techniques is the rammed aggregate pier (RAP) system.

¹Geotechnical Engineering Consultant, ElxisGroup, 54 Vasilissis Sofias Ave., Athens 11528, Greece (corresponding author). ORCID: <https://orcid.org/0000-0001-5561-0058>. Email: g Zalachoris@gmail.com

²Professor, Dept. of Civil and Environmental Engineering, Univ. of California at Berkeley, Davis Hall, Berkeley, CA 94720. ORCID: <https://orcid.org/0000-0001-9907-3362>. Email: zekkos@geoengineer.org

³Assistant Professor, Dept. of Civil and Environmental Engineering, Virginia Polytechnic Institute and State Univ., 111-A Patton Hall, Blacksburg, VA 24061. Email: ayerro@vt.edu

⁴Area Manager–East, Geopier Foundation Company, 130 Harbour Place Drive, Suite 280, Davidson, NC 28036. Email: ABowers@geopier.com

⁵President, Geopier Foundation Company, 130 Harbour Place Drive, Suite 280, Davidson, NC 28036. Email: KWissmann@geopier.com

Note. This manuscript was submitted on February 9, 2022; approved on October 25, 2022; published online on January 3, 2023. Discussion period open until June 3, 2023; separate discussions must be submitted for individual papers. This paper is part of the *Journal of Geotechnical and Geoenvironmental Engineering*, © ASCE, ISSN 1090-0241.

The present study focuses on the rammed aggregate pier system. The technique has been used as an alternative to deep foundations and as a reinforcement for compressible soils (Wissmann et al. 2015) to reduce settlements, mitigate the liquefaction potential, and improve the bearing capacity of foundation systems. Like other compacted stone column methods, RAPs are constructed by compacting crushed aggregate in the ground in vertical lifts. This method is similar to traditional stone column methods from the perspective that the end result is the formation of a compacted column of crushed stone whereby the compaction process changes the initial stress conditions and that the columns of stone are confining stress dependent. As described subsequently, the method is unique from the perspective that the compaction hammer applies vertical tamping instead of horizontal compaction, and the tamper head shape has been designed to enhance construction efficiency. The aggregate can be placed in lifts in a predrilled hole from the surface, after which a hydraulic hammer tamps and compacts the aggregate vertically and horizontally. Alternatively, the aggregate can be placed into the ground using a hollow displacement mandrel with a compaction head on the end. After driving to a specified depth, the mandrel is raised to release the aggregate into the hole and then lowered to compact the aggregate with a high-energy hammer. By repeating the process in relatively thin lifts, a “pier” composed of dense aggregate is constructed. According to previous studies (White et al. 2002, 2007), when constructed this way, aggregate piers exhibit dry densities ranging from 17.6 to 20.3 kg/m³, relative densities of 125%–147%, friction angles on the order of 45°–50°, and dilatancy angles of 6°–11°. The construction of aggregate piers can also alter the in-situ properties of the existing soils by increasing both the relative density and horizontal earth pressure coefficient (Wissmann et al. 2015). A 100% increase in the DMT horizontal stress index, a 200% increase in the dilatometer modulus, and a 100% increase in the cone penetrating testing (CPT) tip resistance were measured in the native soils at distances of 1.5–2.6 m from aggregate piers at a clean loose sand site where aggregate piers were installed (Saftner et al. 2018).

The assessment of the full-scale behavior of densifying ground improvement elements using RAPs under dynamic loading conditions is the focus of the work presented herein. A three-dimensional (3D) computational methodology that leverages full-scale field testing of the ground improvement technique is presented. A detailed description of the steps associated with the present validation study is then provided, and comparisons are made with existing two-dimensional (2D) numerical analyses from the same site. Finally, insights into the physical mechanisms that contribute to the response of the system during dynamic loading through targeted parametric analyses are presented.

The numerical methodology presented herein provides a generalized framework that can be used to study the performance of stone column ground improvement techniques constructed with vibratory probes or other types of compacted aggregate methods if in-situ tested, calibrated, and numerically simulated in a similar manner. It is important to highlight that the specific derived calibrated material parameter values in this paper as well as the particular findings on the contribution of the various mechanisms are affected by the stone column construction technique; hence, they cannot be generalized.

Study Scope and Background

The effectiveness of several ground improvement (GI) methods has been assessed through laboratory studies, centrifuge and numerical modeling, and back-calculations based on case histories

(e.g., Tiznado et al. 2020). However, to the knowledge of the authors, there has not been a comprehensive study combining in-situ site characterization efforts, full-scale field testing, and fully calibrated 3D modeling of the coupled hydromechanical response aimed at the identification of the liquefaction mitigation mechanisms associated with GI methodologies. Consequently, the design of several GI methods is often based on nonvalidated assumptions, making it a challenging task. This study aimed to bridge the gap between full-scale field testing observations, conventional 2D numerical simulations, and full 3D modeling of ground improvement elements as site-tested with the RAP system to gain insights into the mechanisms that contribute to the effectiveness of the GI system, as well as to provide validation of the numerical tools typically employed for computational modeling in engineering practice.

More specifically, this study leveraged data from the full-scale field ground improvement testing (GIT) program executed in Christchurch, New Zealand, and described in detail by Roberts (2017), as well as the insights gained from the 2D fully coupled hydromechanical numerical analyses performed by Thum et al. (2021). This information was combined to inform and evaluate the 3D response of natural and improved ground. The extensive geotechnical and geophysical site investigation data generated during the New Zealand GIT program, detailed documentation of the observed response from the full-scale in-situ experiments, and calibrated baseline constitutive soil model parameters from validated 2D simulations provided a robust framework for the comprehensive assessment of the 3D dynamic response of this ground improvement technique.

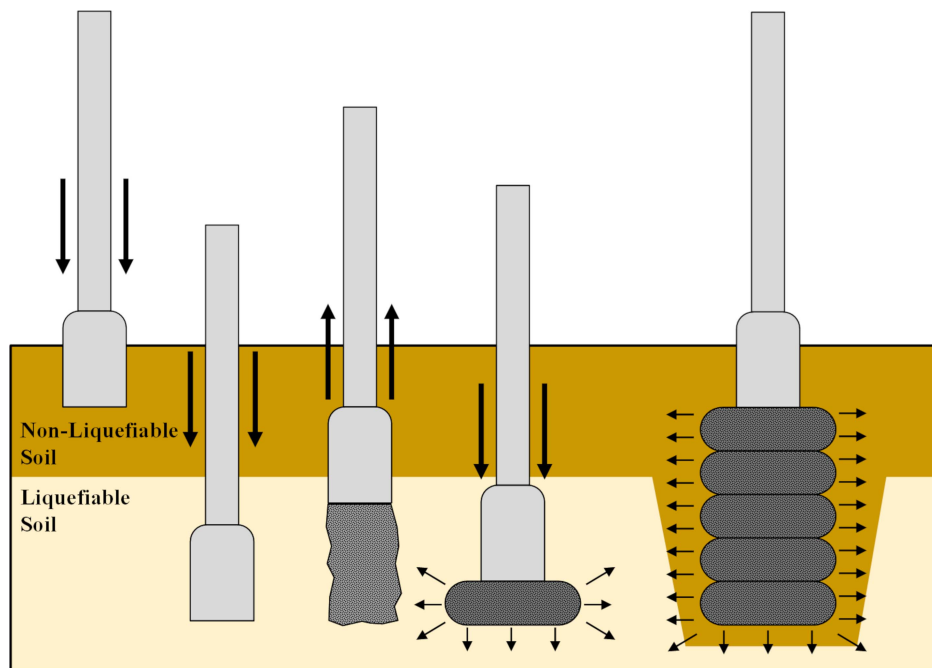
Ground Improvement Testing Program in Christchurch, New Zealand

Following the 2010–2011 Canterbury Earthquake Sequence, the New Zealand Earthquake Commission (EQC) funded a large ground improvement testing study to evaluate and identify shallow ground improvement methods that could increase the liquefaction resistance of granular soils (van Ballegooy et al. 2015). Overall, nine ground improvement methods were field tested, including rapid impact compaction, horizontal soil–cement mixed (HSM) beams, low-mobility grout, and rammed aggregate piers. To comprehensively study these methods, a multitude of full-scale GI test panels at three separate sites in the Christchurch area were developed. At each of the test sites, several in-situ and laboratory site characterization efforts were undertaken, including borings, cone penetrometer tests, direct-push cross-hole (DPCH) tests, dilatometer tests (DMTs), excavation trenches, resonant column (RC) tests, laboratory classifications of soils, and cyclic triaxial tests. These tests aimed at capturing changes in liquefaction resistance caused by the ground improvement techniques employed in comparison to the natural soil. Moreover, shake tests using a vibroseis truck (T-Rex) were used to define the relationship between cyclic shear strain and the generation of excess pore pressure in the field.

Roberts (2017) conducted full-scale testing of natural soil and improved ground using a rammed aggregate pier at three test sites with a vibroseis [Sites 3, 4, and 6; Fig. 1(a)] in Christchurch. These test sites were located within areas that were among the most affected by liquefaction-related damage following the 2010–2011 CES events (Roberts 2017). The constructed rammed aggregate pier system was intended to increase the liquefaction resistance within the top 4 m of the soil profile via a combination of the inclusion of RAP elements with increased permeability, stiffness, and densification of the soil around these RAP elements as a result of installation [Fig. 1(b)]. Ground improvement down to a depth of



(a)



(b)

Fig. 1. (a) Map of Christchurch, New Zealand, with highlighted locations of the sites of the ground improvement testing program and the NNBS strong ground motion station (image © Google, Image © 2021 Terrametrics); and (b) Rammed Aggregate Pier construction methodology.

4 m was decided based on the results of an extensive study in the Christchurch area following the CES events, which concluded that structures founded on nonliquefiable soil layers that reached at least 3 m in depth experienced less structural damage than structures founded on sites without these layers (van Ballegooy et al. 2017). Roberts (2017), based on corrected CPT tip resistance and V_s from DPCH testing, found that rammed aggregate pier elements provided a significant increase in the stiffness of the overall subsurface profile.

At the GIT sites, the RAP piers were installed in a triangular grid pattern with a center-to-center pier spacing of 2 m. Each test area included twenty-two 4-m-long piers, with the diameter of the completed aggregate piers typically being 0.6 m [Fig. 2(b)].

Subsequently, the dynamic response of the natural and improved ground was evaluated using vibroseis shaking (van Ballegooy et al. 2015). T-Rex is a large nees@UTexas mobile shaker used to generate large dynamic forces in three directions (one vertical and two horizontal). The vibroseis truck has diverse force and frequency

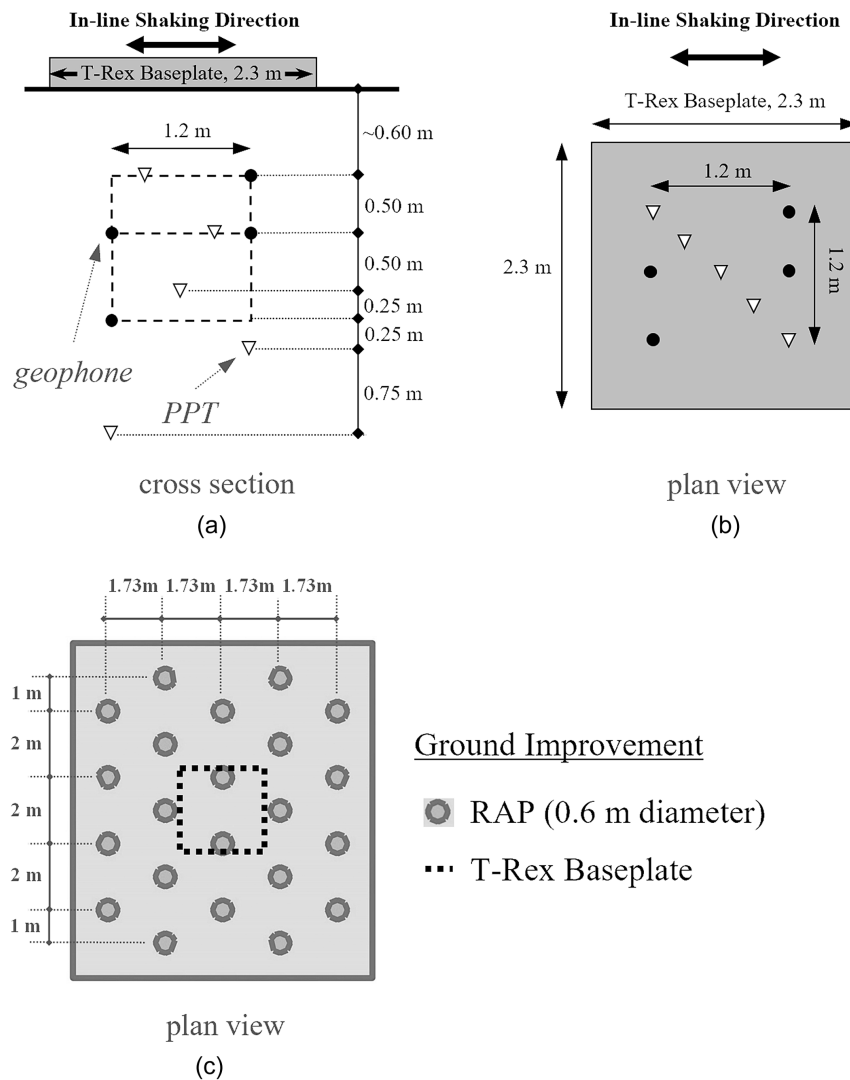


Fig. 2. (a) Cross-section of the instrumentation array used at Site 6 of the ground improvement testing program in Christchurch, New Zealand; (b) plan view of the instrumentation array used at Site 6 of the ground improvement testing program in Christchurch, New Zealand; and (c) plan view of the pier grid layout. (Reprinted with permission from Roberts 2017.)

capabilities and can provide controllable dynamic forces to full-scale systems in the field. Consequently, in-situ measurements of dynamic properties of soil deposits and earth structures can be performed over a wide range of strains, excitation frequencies, number of cycles, and confining pressures. The T-Rex vibroseis is fitted with a 2.3-m-square baseplate, whereas the self-weight of the truck is equal to a vertical load of about 245 kN, corresponding to a static uniform pressure of 46 kPa beneath the baseplate. For the Christchurch testing, dynamic horizontal shaking was applied to the ground with the load ranging from 1.5 to 25 kPa at a frequency of 10 Hz for 100 cycles [Fig. 2(a)]. The sites were instrumented with geophones and pore pressure transducers to capture the propagation of shear waves and the buildup of excess pore pressure within the substrata [Fig. 2(a)] (van Ballegooy et al. 2015; Roberts 2017). Specifically, twenty-eight 2D geophones with a 28-Hz resonance frequency were used to record velocity time histories. From these velocity time histories, shear strains at several depths were estimated. Pore pressure transducers were used to record pore pressures within the soil profile throughout the dynamic loading (Roberts 2017). The stress regime within a soil mass imposed by the loads exerted from a vibroseis truck (such as T-Rex) and

the one resulting from an actual earthquake are different because the loading from an earthquake is typically propagating from depth toward the surface. In contrast, the loading from T-Rex is a concentrated periodic load that propagates from the surface downward (Rathje et al. 2005). Nonetheless, in-situ dynamic testing using vibroseis trucks has proven an effective way to study the full-scale dynamic behavior of a wide range of geomaterials. Alternative methods may involve the use of explosives to simulate an earthquake loading and induce liquefaction (Ashford et al. 2004) or the deployment of long-term seismic monitoring methods to capture and document the in-situ dynamic response of geo-systems in the event of an actual, and sufficiently large, earthquake.

2D Numerical Modeling

Based on the full-scale testing program (Roberts 2017), Thum et al. (2021) performed 2D numerical analyses using model parameters that were calibrated by comparing the computed results with measurements obtained from the well-characterized Test Site 6 [Fig. 1(a)]. Both natural (or unreinforced) and improved (or RAP-reinforced) soil profiles were considered, and the results

were analyzed in terms of shear strains and excess pore water pressures. The analyses performed by Thum et al. (2021) consisted of fully coupled, 2D, hydromechanical simulations using the two-dimensional, explicit finite-difference software Fast Lagrangian Analysis of Continua (FLAC2D) (Itasca 2016). The soil layers were modeled using the advanced sand plasticity constitutive model PM4Sand (version 3.1, Boulanger and Ziotopoulou 2018). The T-Rex shaking scenarios (i.e., top-down shaking) were modeled for different levels of horizontal dynamic shaking consistent with field testing ranging from 1.5 to 25 kPa. The calibrated models for both natural and improved soil profiles were also assessed by subjecting the models to an earthquake time history from the CES events. The east-west component of the North New Brighton School (NNBS) strong motion station recording [Fig. 1(a)] during the M_w 7.1 Darfield earthquake (September 4, 2010) was used because NNBS is located less than 1 km away from Site 6 of the GIT program.

3D Numerical Modeling

Leveraging the aforementioned studies, a numerical evaluation of the three-dimensional response of the natural and improved ground was performed and is discussed herein. The assessment was made using the commercial finite-element codes PLAXIS 2D CONNECT Edition V21 and PLAXIS 3D CONNECT Edition V21, which are commonly employed in engineering practice. Because the constitutive model PM4Sand is not formulated in 3D, the advanced soil model UBC3D-PLM (Galavi et al. 2013), which is a 3D reformulation of that proposed by Beatty and Byrne (2011), typically designated as UBCSand, was used. Similar to the study by Thum et al. (2021), the present validation effort focused on the results from the field test panels at Site 6 of the GIT program [Roberts 2017; Fig. 1(a)].

First, a 2D model was developed in PLAXIS2D using the calibrated PM4Sand model parameters reported by Thum et al. (2021). The analysis (PLAXIS2D-PM4Sand) was validated against the FLAC2D results reported by Thum et al. (2021). Then, UBCSand model parameters were calibrated using single-element undrained cyclic direct simple shear (UCDSS) simulations, and the corresponding 2D numerical results (PLAXIS2D-UBCSand) were validated against the field observations reported by Roberts (2017). Using the calibrated UBCSand parameters and the pier grid pattern shown in Fig. 2(c), 3D models were developed in PLAXIS3D for the following cases: (1) T-Rex top-down shaking on natural soil for different dynamic loading levels; (2) T-Rex top-down shaking on improved soil for different dynamic loading levels; (3) earthquake bottom-up shaking on natural soil using the M_w 7.1 Darfield NNBS station recordings; and (4) earthquake bottom-up shaking on

improved soil using the M_w 7.1 Darfield NNBS station recordings. Finally, the PLAXIS3D models were evaluated against the field observations reported by Roberts (2017).

The following sections present in detail the model geometries, as well as the numerical framework, input dynamic load, and ground motions that provided the basis for the development, calibration, and performance of the computational simulations. The results of these simulations are then discussed and compared to the field observations.

Model Development

For the development of the numerical models, 15-noded triangular plane strain elements in PLAXIS2D and 10-noded volumetric elements in PLAXIS3D were used. The generated model geometries, finite-element meshes, and material zones are illustrated in Figs. 3 and 4 for PLAXIS2D and PLAXIS3D, respectively. To capture a more detailed distribution of strains and stresses at regions of interest, a denser mesh was generated within and around the improved grid zone for both T-Rex (top-down) [Figs. 3 and 4(a and b)] and earthquake (bottom-up) shaking [Figs. 4(c and d)]. All zones below the water table (elevation of -0.5 m) were considered fully saturated. To ensure simultaneous generation and dissipation of excess pore water pressure, consolidation conditions (i.e., fluid flow) throughout dynamic loading in all cases were considered, whereas ground disturbances at the pier-soil interface were neglected for simplification purposes.

Material model properties for the natural and improved soil layers, as well as the pier elements, were selected according to the data and procedures described in Thum et al. (2021). The subsurface conditions at the site (Site 6) generally consisted of silt (ML) overlying silty sand (SM) and clean sand (SW), and the depth to the water table was estimated to be 0.5 m (Thum et al. 2021). All soil layers were simulated using advanced constitutive models (Tables 1 and 2), which will be further discussed in the following sections. The material model properties were calibrated based on the site investigation efforts and field testing reported in Roberts (2017). The initial horizontal effective stresses were set equal to 0.5 times the initial vertical effective stresses. To fully assess the nonlinearities in the dynamic response of the pier elements, parametric analyses were performed where the pier elements were modeled using a field-data-calibrated, cyclic, fully nonlinear constitutive relationship (UBC3D-PLM), with an allowed tension in the pore fluid and a tension limit equal to 100 kPa. The computed shear strains along the centerline of the model, assuming fully nonlinear and linear elastic responses of the RAP elements, were found to be very similar to each other as well as to the measured response, given that the pier elements' response was nearly linear elastic. However, the computational time for the advanced model in the

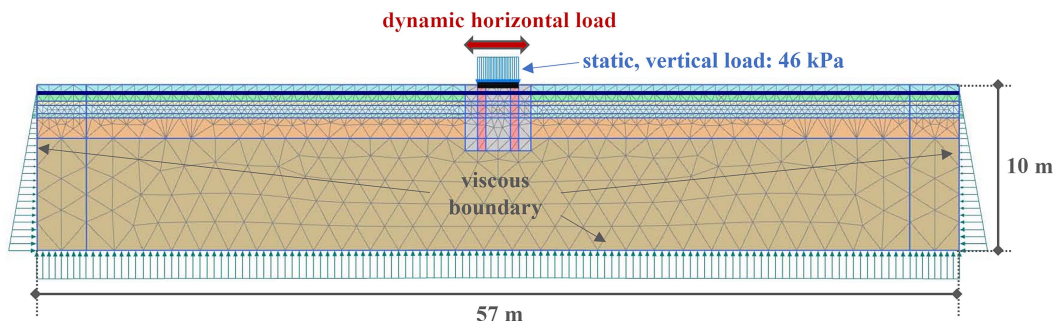


Fig. 3. Developed 2D numerical FE model: improved soil-T-Rex top-down loading case.

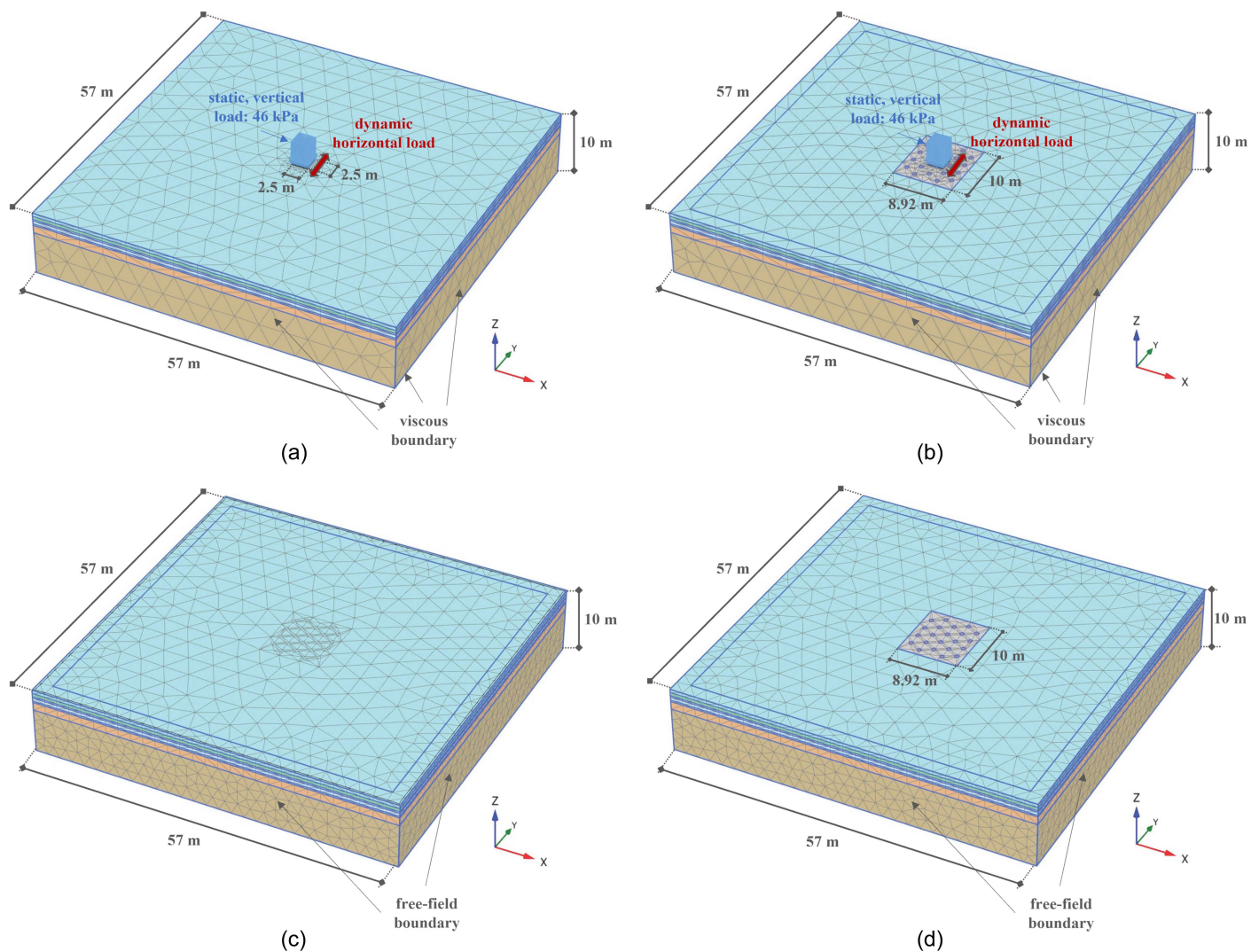


Fig. 4. Developed 3D numerical FE models: (a) natural soil-T-Rex top-down shaking; (b) improved soil-T-Rex top-down shaking; (c) natural soil-earthquake bottom-up loading; and (d) bottom-up earthquake loading.

Table 1. Calibrated UBCSand material properties for the natural, un-reinforced soil layers

Layer	Depth (m)	Fines content (F.C.) (%)	γ (kN/m ³)	$N_{1,60}$	V_S (m/s)	G (MPa)	D_r (%)	k_G^e	k_b	k_G^p	R_f	k_H (m/s)	$\Delta N_{1,60}$	$N_{1,60,CS}$
SP-SM	0–0.5	0	17	10	90	14.9	0.73	699	489	572	0.10	9×10^{-5}	0.0	15.0
ML2	0.5–1.0	96	16	5	94	16.2	0.5	590	413	525	0.73	6×10^{-7}	5.5	15.5
ML1	1.0–1.25	74	18	15	114	23.7	0.33	457	320	253	0.77	6×10^{-7}	5.6	10.6
SM2	1.25–1.75	14	18	25	140	35.9	0.33	457	320	186	0.81	2×10^{-5}	2.9	7.9
SM1	1.75–2.0	14	19	30	151	46.6	0.44	590	413	395	0.75	2×10^{-5}	2.9	12.9
SW2	2.0–3.25	3	19	35	171	59.4	0.42	590	413	277	0.78	2×10^{-5}	0.0	10.0
SW1	3.25–10	3	19	35	179	65.6	0.66	600	420	1,050	0.50	7×10^{-5}	0.0	20.0

Table 2. Calibrated UBCSand material properties for the improved, reinforced soil layers

Layer	Depth (m)	γ (kN/m ³)	V_S (m/s)	G (MPa)	D_r (%)	k_G^e	k_b	k_G^p	R_f	k_H (m/s)	$N_{1,60,CS}$
SP-SM	0–0.5	17	90	14.9	0.64	724	507	450	0.45	9×10^{-5}	10.0
ML2	0.5–1.0	16	94	16.2	0.13	442	309	190	0.99	6×10^{-7}	5.0
ML1	1.0–1.25	18	114	23.7	0.65	525	368	454	0.40	6×10^{-7}	15.0
SM2	1.25–1.75	18	140	35.9	0.79	689	482	1,392	0.10	2×10^{-5}	25.0
SM1	1.75–2.0	19	151	46.6	0.85	835	585	2,355	0.66	2×10^{-5}	30.0
SW2	2.0–3.25	19	171	59.4	0.88	954	668	3,606	0.40	2×10^{-5}	35.0
SW1	3.25–10	19	179	65.6	0.85	1,050	735	3,382	0.90	7×10^{-5}	35.0

Table 3. Linear-elastic material properties for the piers

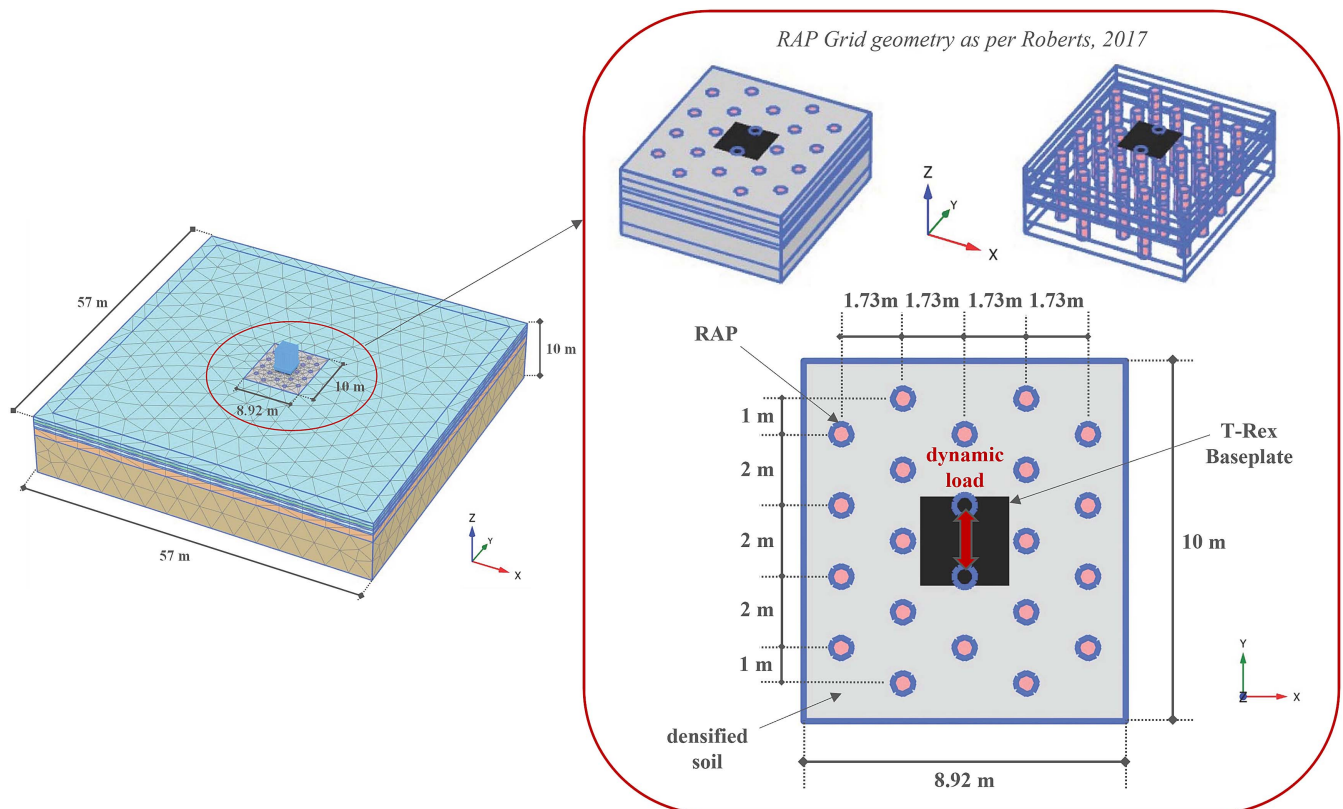
Depth (m)	γ (kN/m ³)	V_S (m/s)	G (MPa)	K (MPa)	ν	k_H (m/s)
0–0.5	20	555	628	5,066	0.30	7×10^{-5}
0.5–1.0	20	307	192	2,840	0.06	7×10^{-5}
1.0–1.25	20	217	96	1,713	0.21	7×10^{-5}
1.25–1.75	20	399	624	13,870	0.41	7×10^{-5}
1.75–2.0	20	574	673	34,478	0.42	7×10^{-5}
2.0–4.0	20	885	1,598	64,096	0.29	7×10^{-5}

RAP elements was significantly greater, and thus we used a linear elastic model (Table 3) for the subsequent analyses.

The pier-improved zones were modeled in accordance with the Thum et al. (2021) simulations and the 3D pier grid geometry, as implemented in the field (Roberts 2017). Consequently, the PLAXIS2D model of the improved profile included (1) two 4-m-long “piers” (panels) with a diameter of 0.5 m, reduced from the actual 0.6 m to account for the 2D modeling of a 3D system, spaced 2 m center to center, and (2) a zone of densified soil surrounding the pier panels extending 0.75 m laterally from the boundaries of the pier elements (Fig. 3). The PLAXIS3D model of the improved soil case included a triangular grid of twenty-two 4-m-long piers with a diameter of 0.6 m and a center-to-center pier spacing of 2 m (Fig. 5). The 0.75-m zone of improved soil laterally from the pier elements is an estimate. It represents the half distance between piers based on measurements, and it is known that there is improvement at that distance from the piers. The improved soil zone also varies as a function of energy input during construction, type of soil, and other factors. Previous studies (e.g., Saftner et al. 2018) indicate a significant improvement extending at distances of up to 2.6 m from the aggregate piers at a clean loose sand site. Thus, the outside perimeter of the improved zone could be larger than the assumed

0.75 m, and a distinct boundary between improved and natural conditions is likely, not present. Still, for simplicity, and given that no additional information exists about this, a 0.75-m-wide improved area along the perimeter was considered in the analysis. The T-Rex baseplate was modeled at the center of the mesh using typical elastic structural steel beam and plate elements with a width of 2.5 m. The static load imposed by the self-weight of the T-Rex vibroseis was simulated by applying a static uniform vertical load of 46 kPa onto the baseplate.

To account for the free-field motion that would exist if the models extended infinitely in the horizontal direction, the lateral boundaries of all models were simulated as “viscous” zones in the case of T-Rex (top–down) shaking, whereas the lateral boundaries of all models were simulated as “free-field” zones in the case of earthquake (bottom–up) shaking, as shown in Figs. 4(a–d), respectively. Therefore, in both cases, the lateral boundaries retained their non-reflecting properties (outward waves were absorbed). Moreover, the lateral boundaries were positioned at a distance from the loaded or central zones such that horizontal displacements at the free field remained negligible. To avoid spurious oscillations at very small deformations, often associated with high-frequency components of motion, small strain, mass-and-stiffness-proportional Rayleigh

**Fig. 5.** Developed 3D model of Rammed Aggregate Piers.

damping equal to $\xi = 0.5\%$ anchored at $f_{\min} = 10$ Hz and $f_{\min} = 1$ Hz was added to the T-Rex (top-down) and earthquake (bottom-up) models, respectively.

Constitutive Soil Models

As mentioned, the cyclic response of the soil layers was simulated using advanced constitutive models. Two constitutive models were used within the framework of the present study: (1) PM4Sand (version 3.1, Boulanger and Ziotopoulou 2018) and (2) UBC3D-PLM (Galavi et al. 2013), the 3D implementation of UBCSand (Beatty and Byrne 2011) (hereafter UBCSand for consistency purposes). A complete discussion on the characteristics of these models is beyond the scope of this paper, which focuses on the model parameters used and the calibration procedure followed.

The PM4Sand model includes default values for most of its input parameters; only three parameters need to be specified: the relative density D_R , the contraction rate parameter h_{p0} , and the shear modulus coefficient G_0 , which is a parameter related to the small-strain shear modulus (G_{\max}). Relative density (D_R) is estimated by correlation to CPT q_c values (Idriss and Boulanger 2008); the coefficient G_0 is obtained by the in-situ shear wave velocity (V_S) measurements because $G_{\max} = \rho \cdot V_S^2$, and h_{p0} is used to modify the soil contractiveness and therefore enable calibration of the models. The UBCSand model has 13 input parameters: the elastic shear stiffness (K_G^e) is defined based on in-situ shear wave velocity (V_S) measurements; model calibration is performed by varying the bulk stiffness (K_b), failure ratio (R_f), or densification factor (f_{dens}) that controls the scaling of the plastic shear modulus during secondary loading, whereas the remaining parameters are estimated using default calibration correlations.

The calibration procedure and obtained model parameters for PM4Sand are discussed extensively in Thum et al. (2021) and therefore are not repeated in detail herein. The model parameters were varied (or “fine-tuned”) until the numerically computed (i.e., 2D analyses in FLAC2D) shear strains and excess pore pressures at various depths resembled the ones estimated by the field test data (Roberts 2017). The calibration procedure for UBCSand involved the variation of model parameters until the response derived from single-element uniform undrained cyclic direct simple shear (UCDSS) simulations at varying levels of cyclic resistance ratio (CRR) values matched the one resulting from similar UCDSS simulations using the field-data-calibrated PM4Sand model. The responses were compared in terms of the stress-strain behavior (cyclic stress ratio CSR versus shear strain γ) and excess pore pressure generation. An example of single-element UCDSS responses using the PM4Sand and UBCSand models for the natural-soil ML2 silt layer is presented in Fig. 6. The calibrated UBCSand model parameters for the associated materials for both natural and improved soil cases analyzed are tabulated in Tables 1 and 2, respectively.

Input Dynamic Loads and Ground Motions

Dynamic excitation was applied at the top and bottom of the models for the T-Rex and earthquake loading cases, respectively. For the T-Rex top-down shaking case, a viscous boundary was assigned along the base of the model in both the x - and y -directions to minimize the effect of reflected waves, whereas for the earthquake bottom-up shaking model, a compliant boundary condition was assumed for the base (i.e., the bedrock was assumed to extend to a significant depth). The T-Rex dynamic horizontal loads were

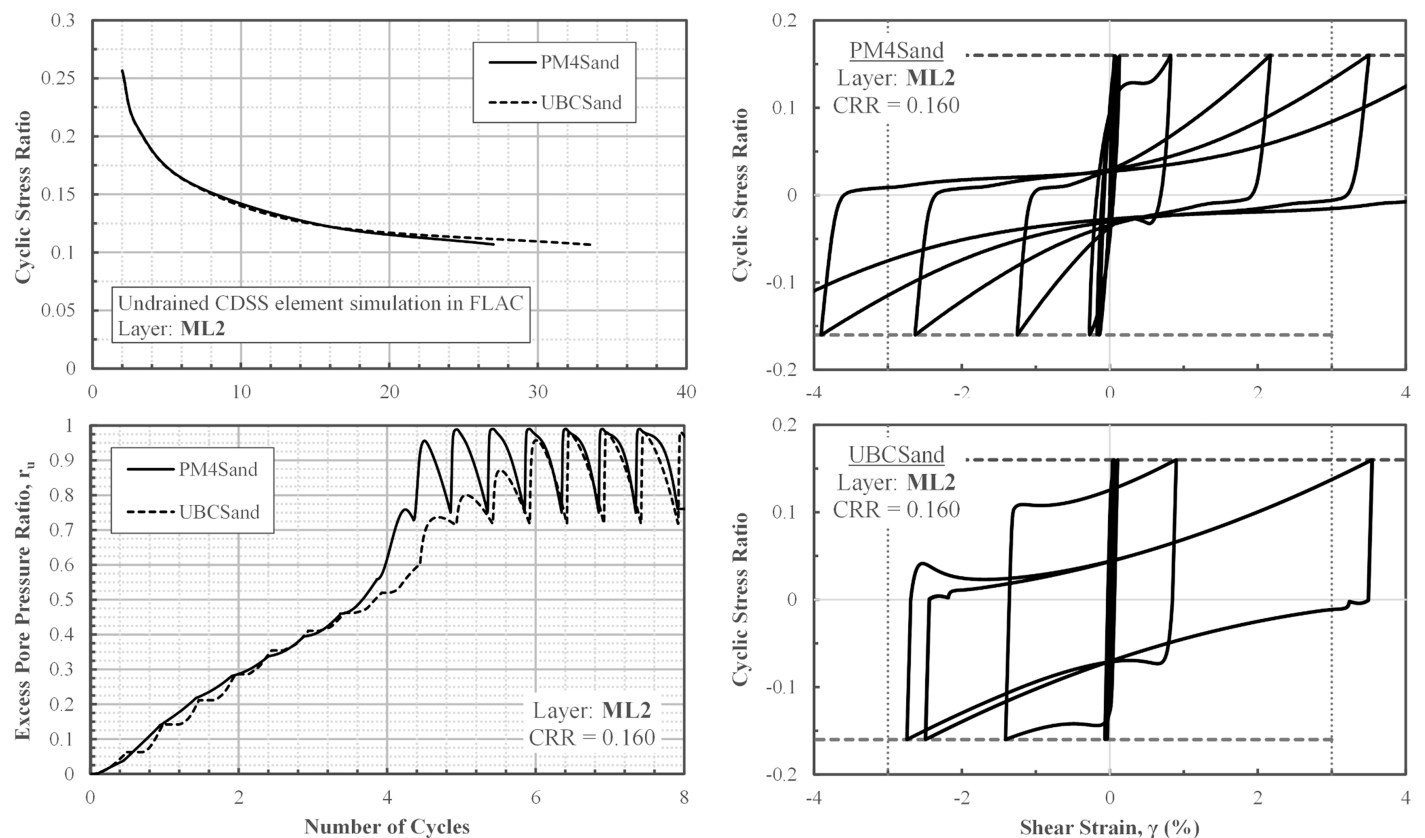


Fig. 6. Response of single-soil elements to undrained cyclic direct simple shear loading: example calibration of PM4Sand and UBCSand parameters for layer ML2.

applied on the modeled T-Rex baseplate as a uniform sinusoidal shear stress with amplitudes of 1.5, 5, and 15 kPa and a frequency of 10 Hz for 100 cycles, similar to the field experiments conducted at Site 6 of the GIT program. For the earthquake models, the input ground motions were applied as velocity time histories $V(t)$ along the base, with only the Incoming Only part of the bedrock velocity time history being considered. The east–west (EW) and north–south (NS) components of the North New Brighton School (NNBS) strong motion station recording [Fig. 1(a)] during the M_w 7.1 Darfield earthquake (September 4, 2010) were used. The time histories for the bottom–up (earthquake) shaking were lowpass filtered at $f_{max} = 25$ Hz. The average element height throughout the entire model (0.4 m) was selected to ensure accurate representation of wave transmission, particularly within and around the RAP-improved grid zone, while optimizing the computational time required for parametric analysis. The maximum element height was equal to 10% of the associated wavelength λ for the soil and RAP elements.

The Incoming Only bedrock velocity time histories corresponding to the EW and NS components of the NNBS recording were

obtained via deconvolution analyses. Reverse one-dimensional (1D) equivalent linear site response analyses were performed using the software STRATA version 0.8.0 (Kottke and Rathje 2008). The recorded EW and NS components of the acceleration records were input at the surface, and the upward propagating waves at the base were computed. For unidirectional shaking, the EW component of the NNBS motion was used, as in Thum et al. (2021). The resulting Incoming Only bedrock velocity time histories and the surface and bedrock outcrop acceleration response spectra are presented in Fig. 7. For simplicity and to reduce the computational cost, the vertical component of the NNBS ground motion was not considered as input.

Results of Numerical Analyses

2D Analyses

Using the 2D model geometries, input T-Rex dynamic loads, and best-estimate calibrated constitutive model parameters presented previously, a series of numerical analyses were performed in

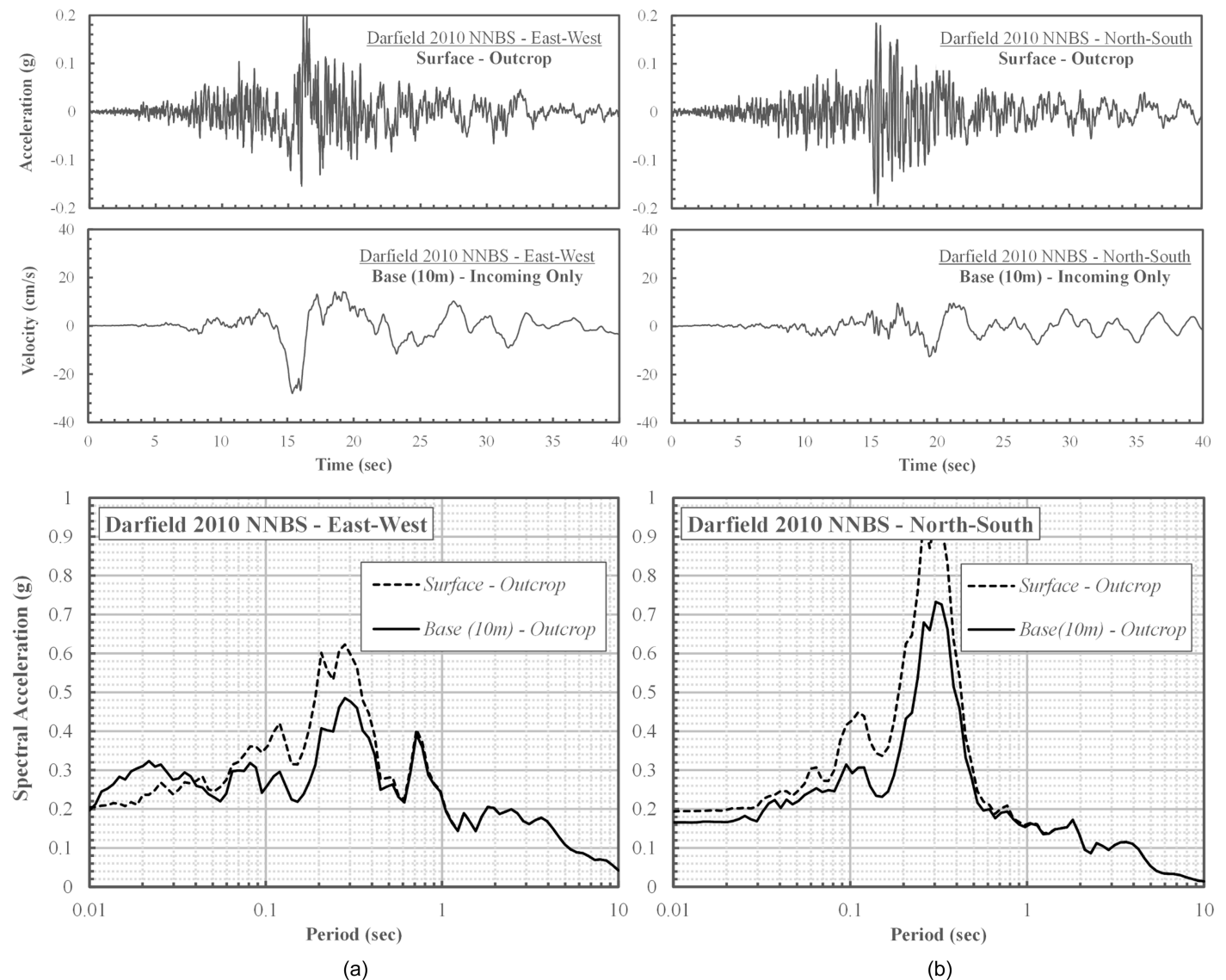


Fig. 7. Deconvolution analyses of Darfield 2010 NNBS ground motions; recorded acceleration time history at the ground surface, incoming-only velocity time history at the base, and bedrock outcrop and surface acceleration response spectra for (a) east–west component; and (b) north–south component.

PLAXIS2D, simulating the in-situ T-Rex top-down shaking experiments on the improved soil profiles. The PLAXIS2D results, in terms of contours of the excess pore pressure ratio (r_u) at the end of shaking for all dynamic load levels, are presented in Fig. 8 for the UBCSand model. The r_u contours in Fig. 8 illustrate the obvious effect of the intensity of shaking on the generation of excess pore pressures throughout the model, with substantial zones having $r_u > 0.7$ for the case of the T-Rex 15 kPa load. The presence of the piers as well as the densification of the surrounding soil resulted in zones with elevated r_u values away from the ground-improved zone.

To evaluate and validate the PLAXIS2D simulation parameters, the shear strains γ , computed along the centerline of the model, below the T-Rex baseplate, were compared to the ones reported by Thum et al. (2021) (FLAC2D) and the field observations (Roberts 2017). As shown in Fig. 9(a), for the improved-soil T-Rex 5 kPa case, both PLAXIS2D models (PM4Sand and UBCSand) compared relatively well with each other as well as with FLAC2D, indicating a successful calibration of the UBCSand model against the PM4Sand single-element UCDS response. Moreover, the

dynamic response produced by the three 2D models (FLAC2D, PLAXIS2D-PM4Sand, and PLAXIS2D-UBCSand) was also assessed in terms of the computed r_u time histories at five depths of the improved soil layers directly below the T-Rex baseplate (Fig. 10). Similar to the shear strain distributions with depth, the r_u time histories showed substantial similarities between the three 2D models for all depths depicted in Fig. 10, with PLAXIS2D-PM4Sand resulting in a slightly more rapid and pronounced generation of excess pore pressures. Thereafter, the PLAXIS2D-UBCSand model was further validated by comparing the numerically obtained shear strains γ at different depths with the field data for all T-Rex dynamic loads considered [Fig. 9(b)]. Once again, the effect of the intensity of shaking was evident, with significantly higher shear strain values for the case of T-Rex 15-kPa load compared to lower load levels [Fig. 9(b)]. The PLAXIS-UBCSand model produced responses similar to the observations, with a slight underestimation of shear strains for the T-Rex 1.5 kPa load at depths less than 2 m and an overestimation for the T-Rex 15 kPa load at depths less than 1.5 m. The trends presented herein are similar to their counterparts obtained by Thum et al. (2021).

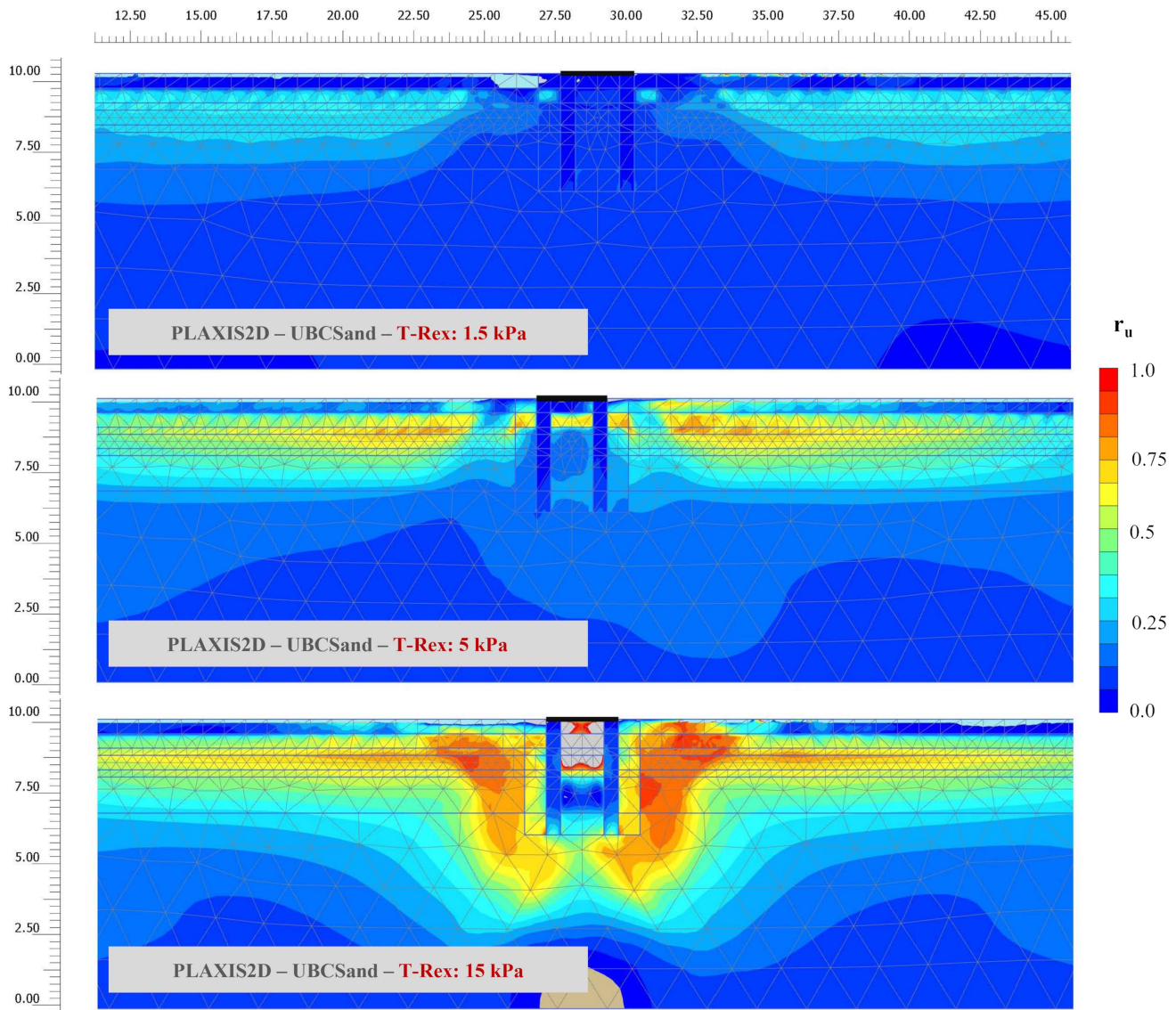


Fig. 8. Computed excess pore pressure ratio r_u values of the PLAXIS2D model for T-Rex top-down shaking of 1, 5, and 15 kPa: UBCSand.

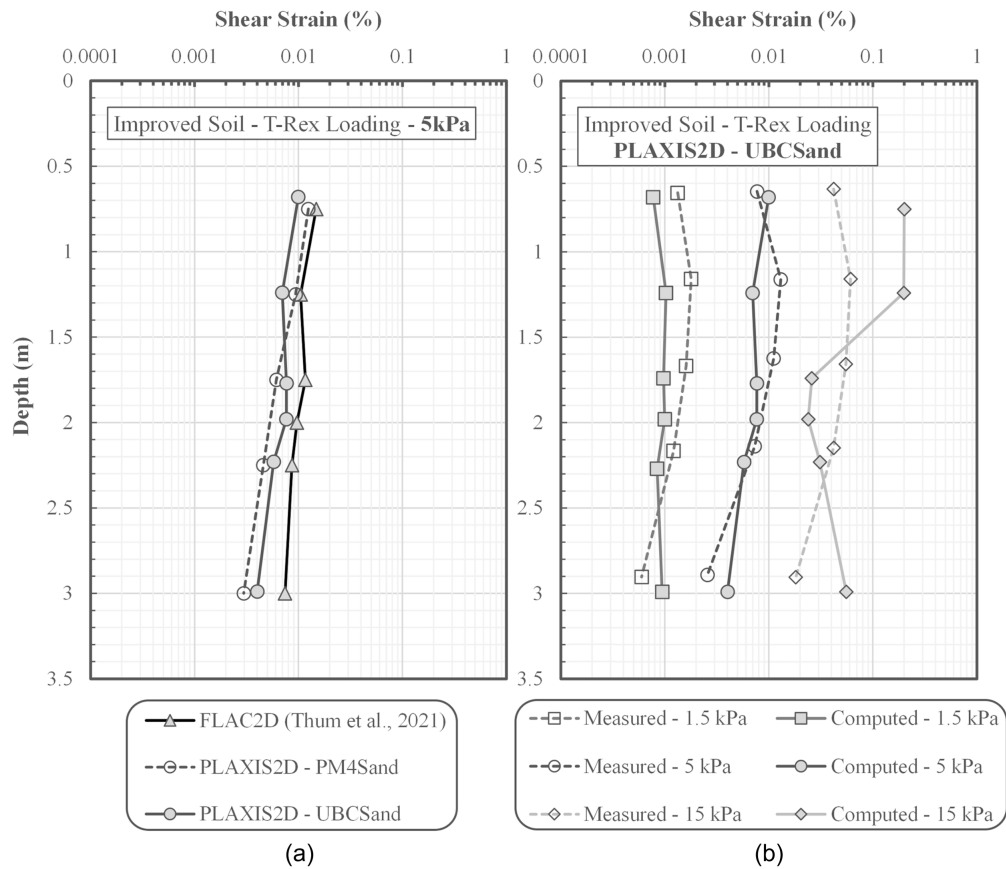


Fig. 9. Shear strains γ_{yz} along the centerline of the 2D model: (a) comparison between numerical models for improved soil-T-Rex top-down shaking of 5 kPa; and (b) comparison between observed and computed responses for improved soil-T-Rex top-down shaking.

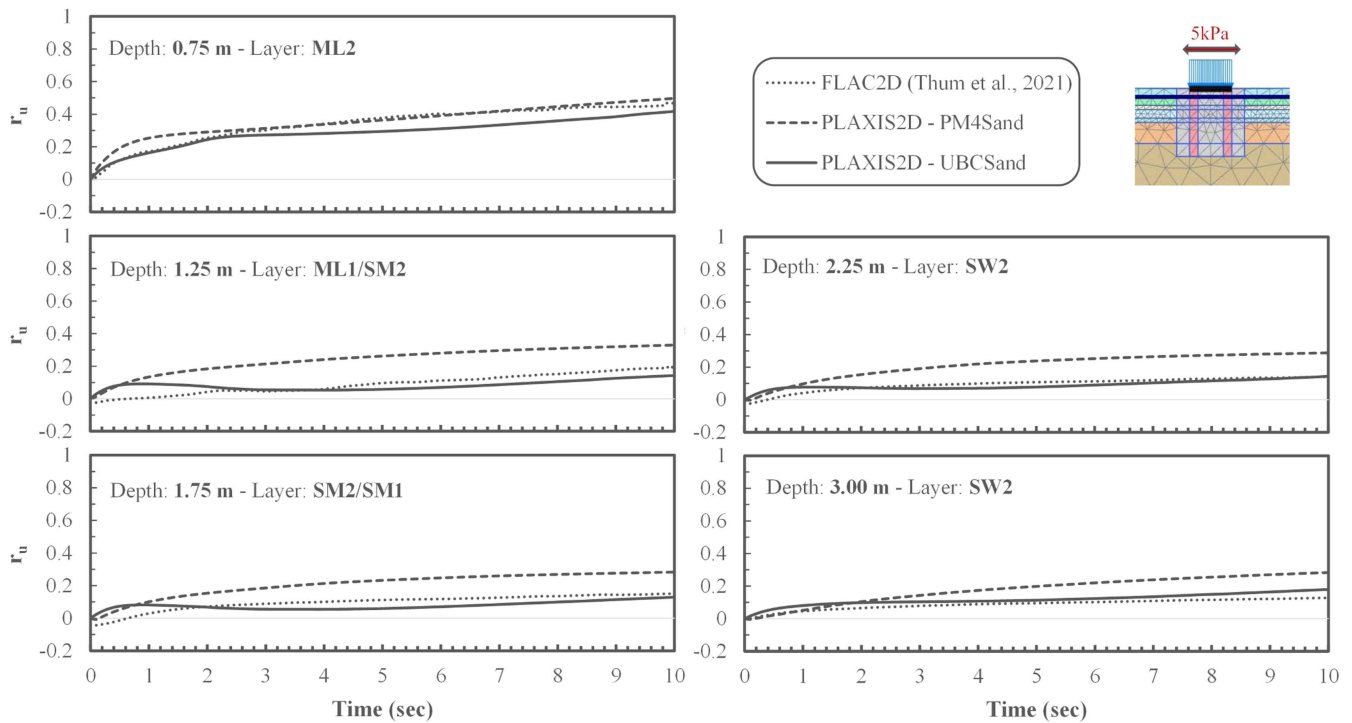


Fig. 10. Computed r_u values at stress points along the centerline of the 2D model for improved soil-T-Rex top-down shaking of 5 kPa; comparison between FLAC2D (Thum et al. 2021), PLAXIS2D-PM4Sand, and PLAXIS2D-UBCSand.

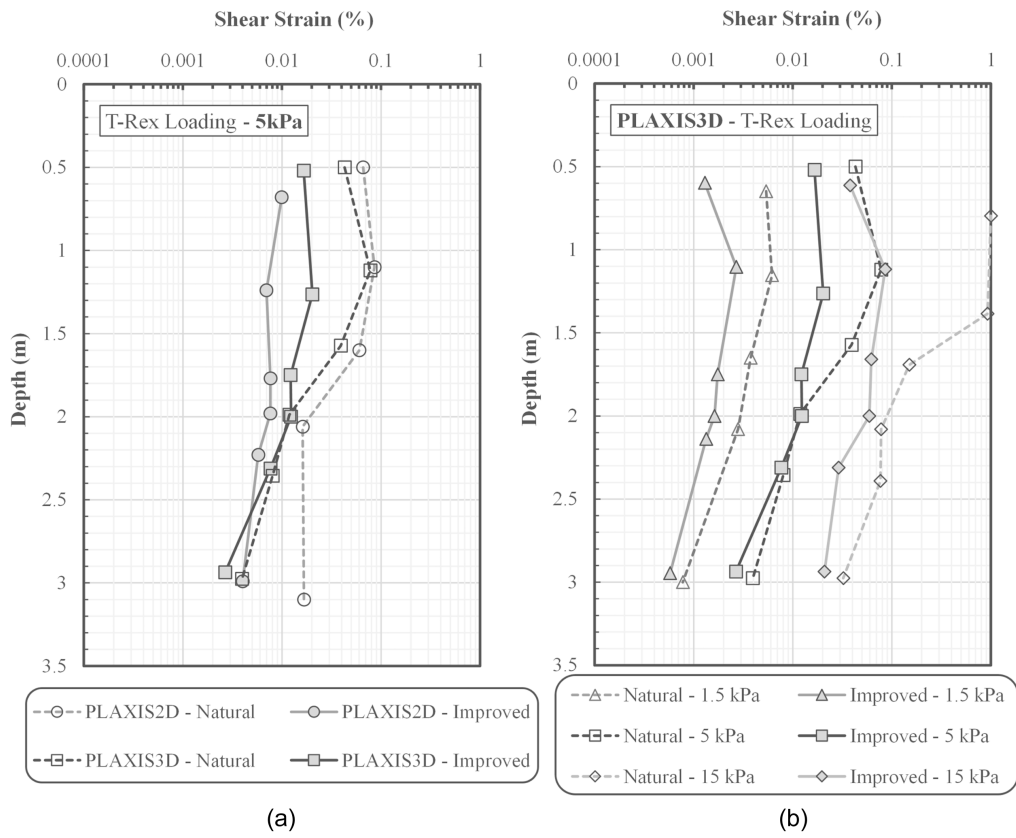


Fig. 11. Computed shear strains γ_{yz} along the centerline of the model for T-Rex top-down shaking: (a) comparison between 2D and 3D numerical models for improved and natural soil for T-Rex shaking of 5 kPa; and (b) comparison between improved and natural soil cases for all T-Rex top-down shaking loads.

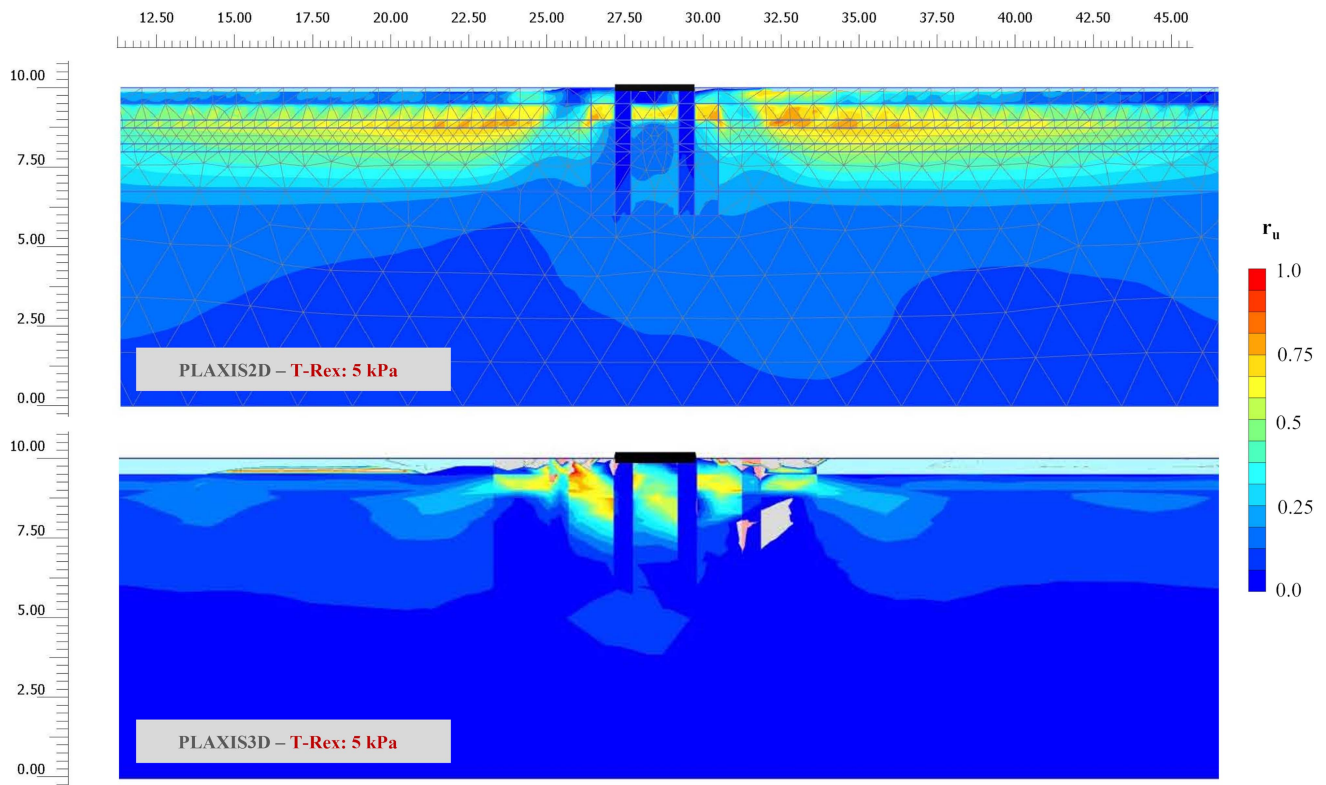


Fig. 12. Computed excess pore pressure ratio r_u values for improved-soil T-Rex top-down shaking of 5 kPa; comparison between 2D and 3D numerical models.

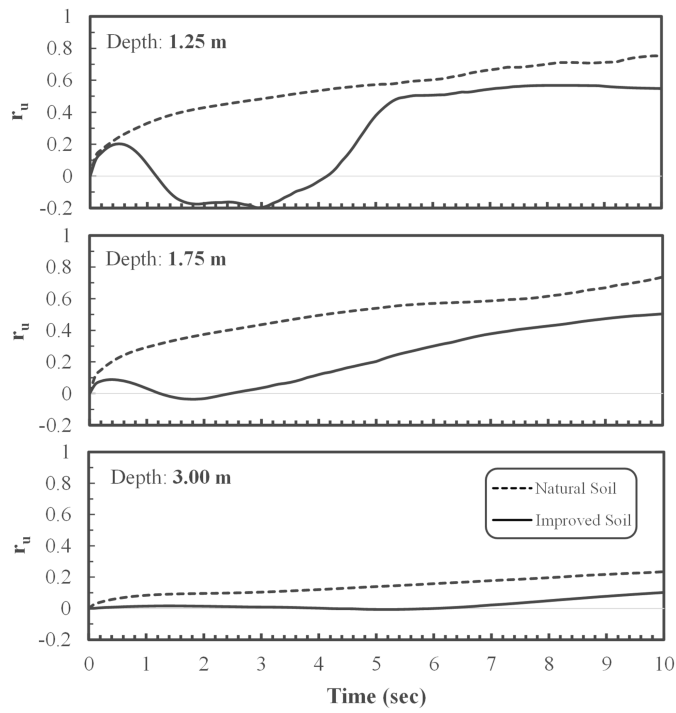


Fig. 13. Computed r_u values at stress points along the centerline of the PLAXIS3D model for T-Rex top-down shaking of 5 kPa; comparison between improved and natural soil cases.

3D Numerical Analyses

Having calibrated the UBCSand model parameters against data from in-situ experiments and well-documented 2D numerical analyses, fully coupled effective stress 3D simulations of the dynamic response of the natural and improved soil, as described previously (Figs. 4 and 5), were performed to assess the 3D behavior of densifying ground improvement elements, as tested in the field. The computed responses were evaluated in terms of shear strain distributions with depth along the centerline of the models, as well as excess pore pressure generation. Initially, the PLAXIS3D model results were compared with PLAXIS2D; for example, for the natural and RAP-improved T-Rex 5-kPa load cases, the 2D-computed and 3D-computed shear strains matched relatively well, with some noticeable differences [Fig. 11(a)]. More specifically, the 3D natural soil model produced 50% lower γ values at depths greater than 2 m compared to its 2D counterpart, whereas the 3D improved soil model gave slightly greater shear strains than the corresponding 2D model at depths less than 2 m [Fig. 11(a)]. Both these observations may be associated with the effect of 3D wave propagation. The 3D constructive interference of shear waves near the dynamic source can lead to greater deformations at shallower strata, whereas energy dissipation through 3D radiation damping may be associated with lower shear strains at greater depths. Moreover, load transferring through the 3D grid of pier elements may lead to a more representative 3D stress regime, especially within the upper soil layers. Finally, by comparing the PLAXIS2D and PLAXIS3D r_u contours at the end of shaking for the improved-soil

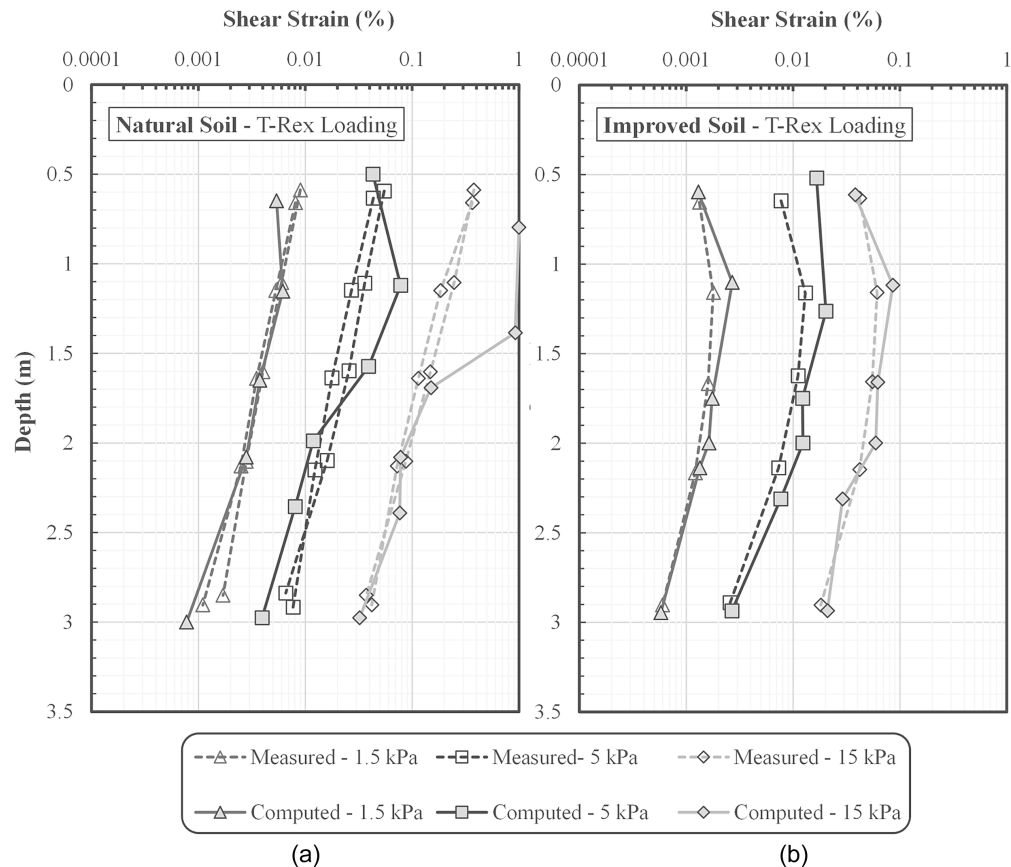


Fig. 14. Computed shear strains γ_{yz} along the centerline of the model for T-Rex top-down shaking and all dynamic loading levels considered: (a) comparison between 3D numerical models and field data-based estimations for the natural soil cases (two field test panels); and (b) comparison between 3D numerical models and field data-based estimations for the improved soil cases.

T-Rex 5-kPa load case (Fig. 12), it is observed that the full 3D modeling of the piers and densified soil limited the zones of excess pore pressure generation within a narrower area; that is, the PLAXIS3D model showed smaller r_u values away from the ground-improved zone compared to PLAXIS 2D (Fig. 12).

The effect of densifying ground improvement elements on the dynamically induced behavior of liquefiable strata is evident in the 3D numerical responses of the natural and improved soil models [Figs. 11(b) and 13]. The ground improvement reduced the generated shear strains along the centerline of the models for all T-Rex loading levels [Fig. 11(b)], with the largest effect of soil improvement seen at shallower depths (less than 2 m). The ground improvement methodology was shown to reduce the generation of excess pore pressures at all depths, with the computed r_u values within the improved soil profiles being, on average, 30%–50% smaller than the r_u values within the natural soils throughout the duration of shaking (Fig. 13). The latter remark is more consequential at shallower depths (less than 2 m), where, due to the proximity to the T-Rex dynamic source, greater excess pore pressures developed (Fig. 13). A more detailed investigation of the predominant mechanisms contributing to the dynamic response of the ground improvement method will be presented in following sections.

The PLAXIS3D simulation results were also validated against the observations documented in the field (Roberts 2017). Figs. 14 and 15 present the comparisons of the 3D numerically obtained results with the field data-based observations for the natural and improved soil profiles subjected to three levels of T-Rex dynamic loading (1.5, 5, and 15 kPa). Fig. 14 shows the comparison in terms of shear strain distribution with depth, and Fig. 15 depicts the corresponding r_u – γ relationships characterizing the response of strata at different depths. Based on Fig. 14, it is evident that the numerically estimated shear strains matched relatively well the measured values both for the natural profile [Fig. 14(a)] and especially the improved [Fig. 14(b)] soil profile. A slight but noticeable deviation from the measured γ values was seen for the natural-soil T-Rex 15-kPa load case at depths less than 1.5 m; that is, the 3D finite-element analysis produced shear strain values of about 1%, whereas the in-situ measurements corresponded to shear strains of 0.2%–0.4%. Such overestimation is possibly attributed to a relatively poor calibration of the UBCSand model parameters for the ML1 and ML2 layers at lower CRR values or greater number of UCDS

cycles (Fig. 6). Nonetheless, the numerically estimated PLAXIS3D shear strains for the improved soil profile more favorably agreed with the in-situ data [Fig. 14(b)] compared to the corresponding PLAXIS2D analyses results [Fig. 9(b)]. This observation also emphasizes the effect of 3D wave propagation, that is, the 3D constructive interference of shear waves near the dynamic source and energy dissipation through 3D radiation damping. Finally, similar observations can be made by comparing the computed and measured relationships between cyclic shear strain and the generation of excess pore pressures at different depths (Fig. 15); that is, the numerical results matched reasonably well with the field measurements presented by Roberts (2017). However, particularly for the natural soil case, the predicted r_u values were slightly higher than the measured values at each shear strain amplitude, possibly indicating a more rapid dissipation mechanism of excess pore pressures in the field due to higher in-situ soil permeabilities than the ones considered in this study or the presence of lateral soil layer variability. Nonetheless, it can be argued that, based on both Figs. 14 and 15, the 3D numerical models developed and analyzed herein for both natural and improved soil cases were validated vis-à-vis the field observations.

Effect of Bidirectional Shaking

The field testing performance of the ground improvement methodology was further assessed by subjecting the developed 3D natural and improved soil models to the horizontal components of the September 4, 2010, M_w 7.1 Darfield NNBS station recordings. To evaluate the effect of the multidirectional nature of the actual seismic loading, initially, the 3D models were subjected to a unidirectional shaking scenario, where only the EW component of the NNBS record was used (Fig. 7). Thereafter, the deconvolved Incoming Only velocity time series of both the EW and NS components of the NNBS record (Fig. 7) was used as input in the y - and x -directions, respectively, simulating a bidirectional shaking scenario.

Fig. 16 presents the PLAXIS3D computed r_u contours around the center zones of the model down to a depth of 4 m at three instances ($t = 15, 25,$ and 40 sec) during the earthquake shaking for the natural [Figs. 16(a and c)] and improved [Figs. 16(b and d)] soil cases and for both unidirectional [Figs. 16(a and b)] and

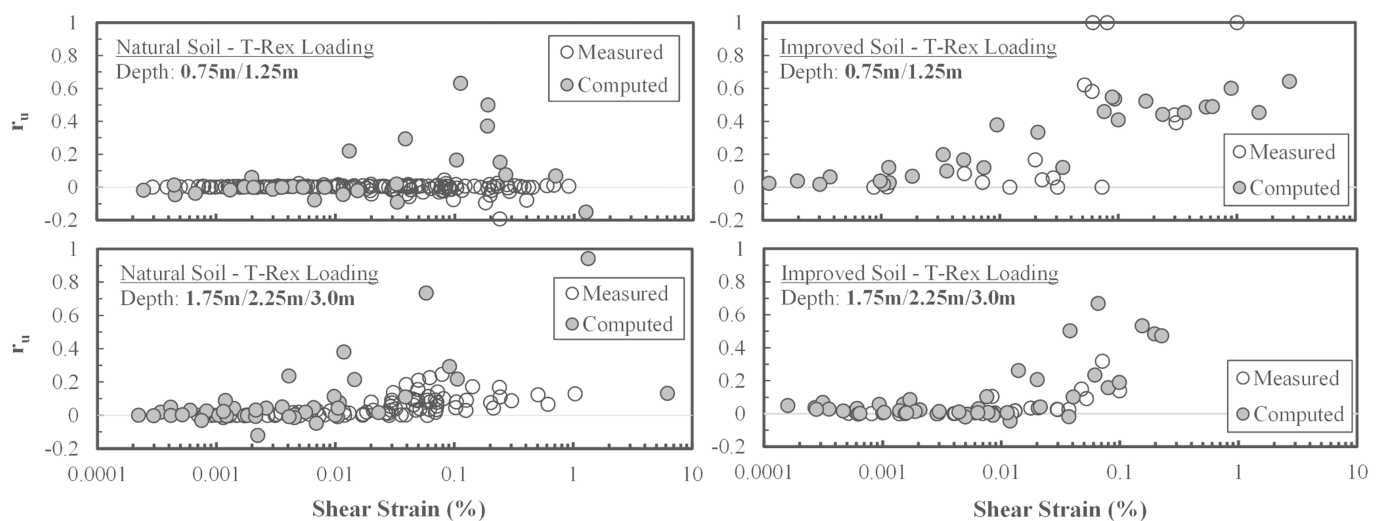


Fig. 15. Excess pore pressure ratio r_u versus shear strains γ_{yz} along the centerline for T-Rex top-down shaking; comparison between observed (Roberts 2017) and computed PLAXIS3D responses for both natural and improved soil cases.

bidirectional [Figs. 16(c and d)] seismic loading scenarios. To improve data visualization, the upper SP-SM layer, which was above the water table and considered unsaturated, is not depicted in Fig. 16. As seen in Fig. 16, zones of significant excess pore pressure buildup ($r_u > 0.7$) were evident at $t = 25$ sec and $t = 40$ sec for all cases and earthquake loads. In contrast, at $t = 15$ sec, only the improved models showed some excess pore pressure buildup ($r_u > 0.3-0.5$) within the densified ML2 layer, that is, at depth 0.5–1.0 m. Nonetheless, at $t = 25$ sec and $t = 40$ sec, the natural soil models presented extensive liquefied zones [Figs. 16(a and c)] compared to the improved models [Figs. 16(b and d)], signifying

the effectiveness of the ground improvement in liquefaction mitigation. Furthermore, the results of the PLAXIS3D analyses for the natural soil profile were consistent with field observations (van Ballegooy et al. 2015) that indicated that the site liquefied following the September 4, 2010, $M_w 7.1$ Darfield event.

Fig. 16 also illustrates the effect of multidirectional shaking on liquefaction triggering. Bidirectional earthquake shaking resulted in substantially more pronounced liquefied zones at $t = 25$ sec and $t = 40$ sec. This seemed particularly pronounced for the natural soil cases [Figs. 16(a and c)], whereas it was more subtle for the improved soil cases [Figs. 16(b and d)]. To further validate this

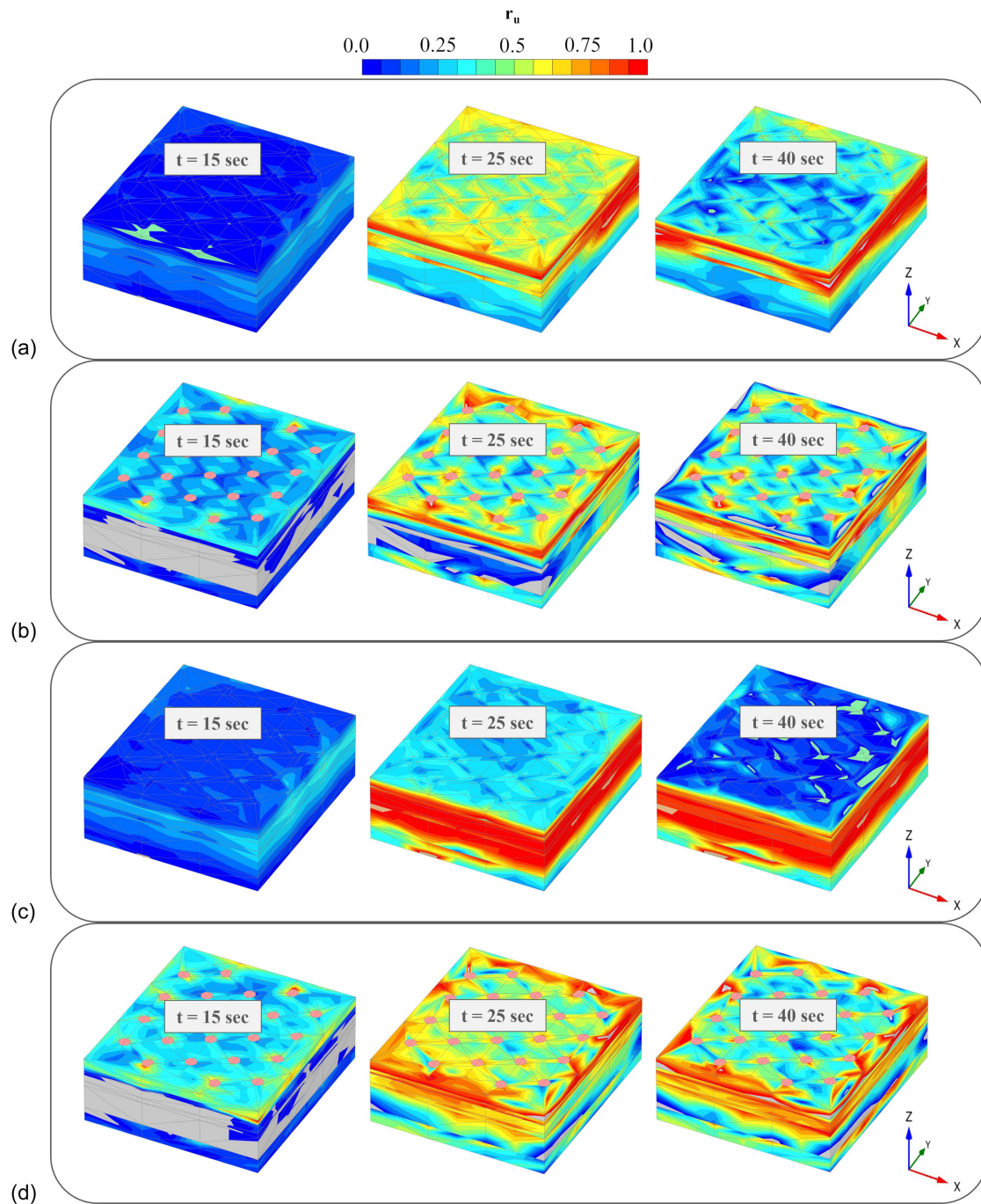


Fig. 16. Computed r_u values around the center point of the PLAXIS3D model at different instants of earthquake bottom-up shaking: (a) natural soil–unidirectional shaking; (b) improved soil–single-directional shaking; (c) natural soil–bidirectional shaking; and (d) improved soil–bidirectional shaking.

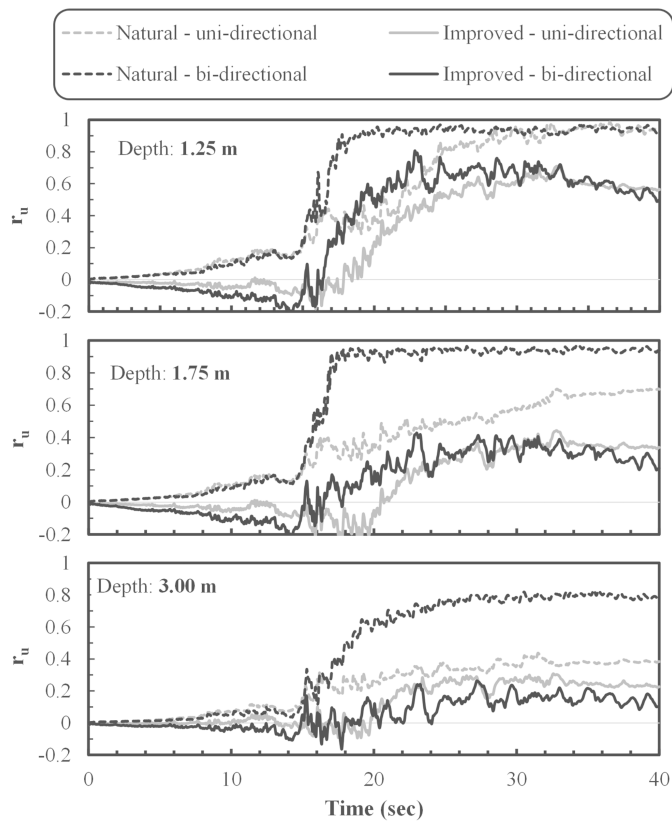


Fig. 17. Computed r_u time histories at stress points along the centerline of the PLAXIS3D model for earthquake bottom-up shaking; comparison between improved and natural soil cases with unidirectional and bidirectional shaking.

observation, Fig. 17 shows the computed r_u time histories at three depths along the centerline of the models (1.25, 1.75, and 3.0 m) for the natural and improved soil cases and both unidirectional and bidirectional earthquake loading. Bidirectional shaking was associated with the rapid development of excess pore pressures at $t > 16$ s, particularly for the natural soil case (Fig. 17). These findings are in line with previous studies, which have consistently shown that multidirectional shaking increases the liquefaction potential of soil (e.g., Pyke et al. 1975; Seed et al. 1975, 2003; Kammerer et al. 2004). Nonetheless, multidirectional shaking imposes stress paths that are not reproduced in a single-element test on which the calibration procedure presented earlier is based.

The 3D response of the improved ground was also evaluated by comparing the natural and improved soil models in terms of shear strain distribution with depth (Fig. 18) using both single and bidirectional seismic inputs. Although the improved ground simulations indicated systematically smaller shear strain values, the reduction of dynamically induced shear deformations appeared more significant for bidirectional shaking [Fig. 18(a)]. This observation may indicate an enhanced pier-soil interaction in three dimensions, whereas the shear strains depicted in Fig. 18(a) are estimated along a plane in the direction of the EW NNBS ground motion, which may not necessarily correspond to the plane experiencing the greatest shear strains in the case of bidirectional shaking. Moreover, Fig. 18(b) compares the shear strain responses between the PLAXIS3D bidirectional shaking models with the ones reported by Thum et al. (2021), who used, as input to their FLAC2D model, the deconvolved EW NNBS record scaled by a factor of 1.11 to indirectly account for the influence of multidirectional shaking on liquefaction triggering. Based on Fig. 18(b), and even though bidirectional shaking in PLAXIS3D results in greater shear strains than FLAC2D for the natural soil model, the scaled

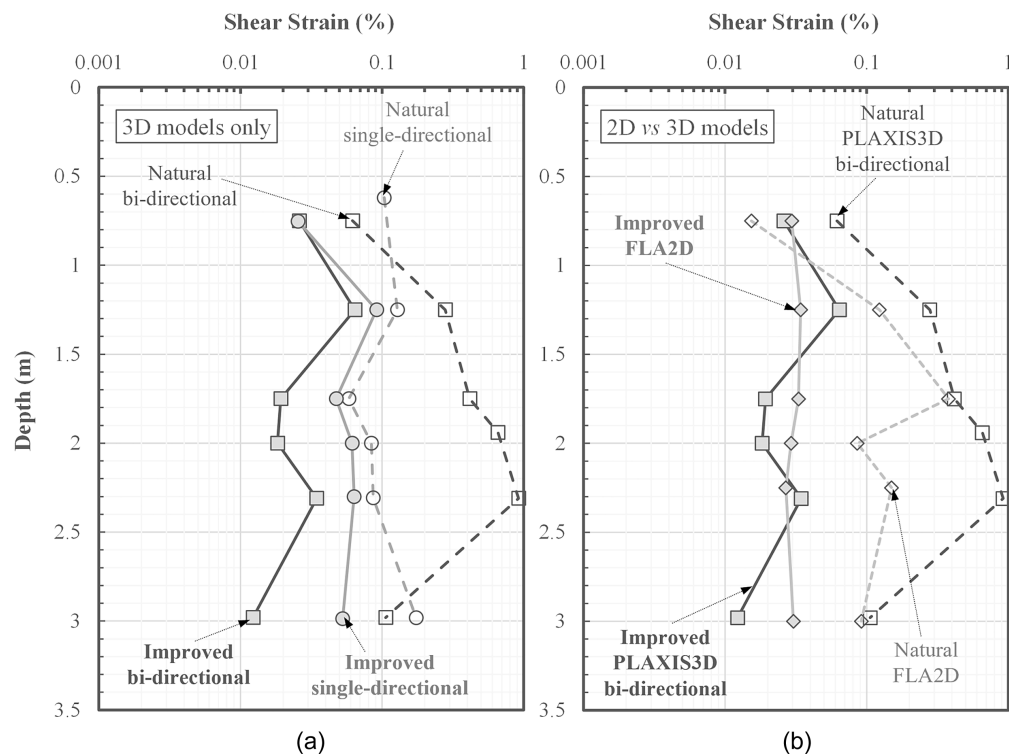


Fig. 18. Computed shear strains γ_{yz} along the centerline of the model for earthquake bottom-up shaking: (a) comparison between 3D numerical models with unidirectional and bidirectional shaking; and (b) comparison between scaled 2D (Thum et al. 2021) and 3D numerical models with bidirectional shaking.

motion was closer to the PLAXIS3D bidirectional shaking than the PLAXIS3D model with unidirectional unscaled shaking [Fig. 18(a)]. Finally, Fig. 19 presents the relationships between cyclic shear strain and the generation of excess pore pressures for the natural and improved soil profiles at different depths. Estimations of best-fit lines have been fit to the data, aggregated within two depth categories (Roberts 2017; Thum et al. 2021): (1) 0.75 and 1.25 m; and (2) 1.75, 2.25, and 3.0 m. Based on Fig. 19, bidirectional shaking was seen to cause an increase in the developed cyclic shear strains, particularly in the deeper natural soil layers, without substantially altering their overall trend; that is, the r_u - γ relationships describing the best-fit line estimations remained approximately the same in all cases.

Mechanisms of Ground Improvement

Additional simulations were performed in an attempt to isolate the different mechanisms contributing to the numerically obtained response of the improved ground subjected to earthquake shaking. In these parametric analyses, the effects of the (1) permeability of the piers, (2) shear stiffness of the piers, (3) densification of the soil caused by the pier installation, and (4) lateral earth pressures within the densified soil were investigated. More specifically, in addition to the baseline model case, as described by the material and model properties tabulated in Tables 2 and 3, the 3D response of the system was evaluated by using: (1) pier permeability ($k_{H,RAP}$) values of 10^{-3} and 10^{-7} m/s, (2) shear wave velocities throughout the piers ($V_{S,RAP}$) of more than 600 and less than 250 m/s, (3) relative densities (D_R) of the improved soil of at least 80% and equal to the natural soil values (Table 1) (i.e., no densification), and (4) lateral earth pressure coefficient (K_0) values of the densified soil equal to 1.0, 0.65, and 0.35. All simulations were performed under bidirectional earthquake shaking using the Darfield 2010 NNBS records (Fig. 7). Fig. 20 depicts the numerically obtained shear strain and r_u distributions with depth along the centerline of the model for all parametric analyses considered.

The numerical results of the aforementioned analyses (Fig. 20) indicate that the mechanisms that predominantly contribute to the reduction of shear deformations and pore pressure generation within the soil profile are: (1) soil densification [Fig. 20(c)]; and

(2) lateral pressure increase [Fig. 20(d)], both being a consequence of the pier installation process. As shown in Fig. 20, the improved soil profiles experienced similar cyclic shear strains regardless of the considered permeability and shear stiffness of the pier elements [Figs. 20(a and b), respectively]. A small ($\sim 10\%$ – 20%) reduction in the generated r_u values was only observed when a relatively large hydraulic conductivity was considered for the pier elements [$k_{H,RAP} = 10^{-3}$ m/s, Fig. 20(a)] compared to the baseline scenario (i.e., $k_{H,RAP} = 7 \cdot 10^{-5}$ m/s, Table 3), due to a more rapid dissipation of excess pore water pressures. The shear stiffness of the pier elements did not appear to have a distinguishable effect on the modeled response of the densified soil [Fig. 20(b)]. Contrarily, different degrees of densification of the soil surrounding the pier elements were shown to have a significant effect on the computed shear deformation along the centerline of the model, as well as on the pore water pressure generation. When a denser soil profile was considered (i.e., $D_R \geq 80\%$) for the improved soil layers compared to the baseline case, both cyclic shear strains and r_u values were reduced at depths less than 2 m [Fig. 20(c)]. If no soil densification was achieved following the installation of the piers [i.e., the “no densification” case in Fig. 20(c)], the exhibited shear strains and excess pore pressures were significantly greater than the baseline case, with shear strains consistently greater than 0.1% and $r_u > 0.7$ throughout the soil profile [Fig. 20(c)]. Finally, based on the results of the parametric analyses, an increase in the lateral earth pressures within the densified soil (i.e., $K_0 = 0.65$ and $K_0 = 1.0$) reduced the computed shear strains along the entire depth of the improved zone [Fig. 20(d)]. The earth pressure coefficient at rest (K_0) had a secondary effect on the generated excess pore pressures when $K_0 = 0.65$, whereas the numerical model with $K_0 = 1.0$ produced approximately 50% smaller r_u values throughout the improved soil profile [Fig. 20(d)]. These observations show that densification increased the liquefaction resistance of the soil profile, leading to lower cyclic shear strains and excess pore pressures. Moreover, it was observed that the increase in the lateral earth pressures within the densified zone also contributed to the reduction of the exhibited shear deformations and excess pore water pressures, particularly for $K_0 = 1.0$. The focus of the previous discussion was on the assessment of the influence of these mechanisms on the pore pressure response and the induced shear strains along the centerline of the

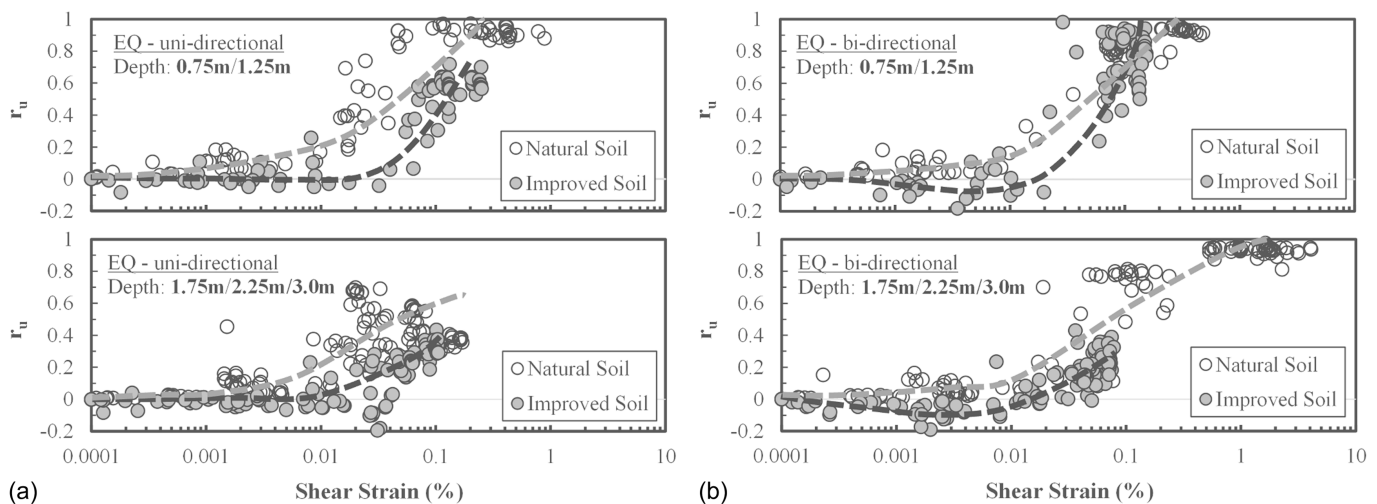


Fig. 19. Excess pore pressure ratio r_u versus shear strains γ_{yz} along the centerline of the PLAXIS3D model for earthquake bottom-up shaking: (a) comparison between natural and improved soil cases with unidirectional shaking; and (b) comparison between natural and improved soil cases with bidirectional shaking. Dashed lines represent estimates of the best-fit lines to the data: light grey for natural soil cases and dark grey for improved soil cases.

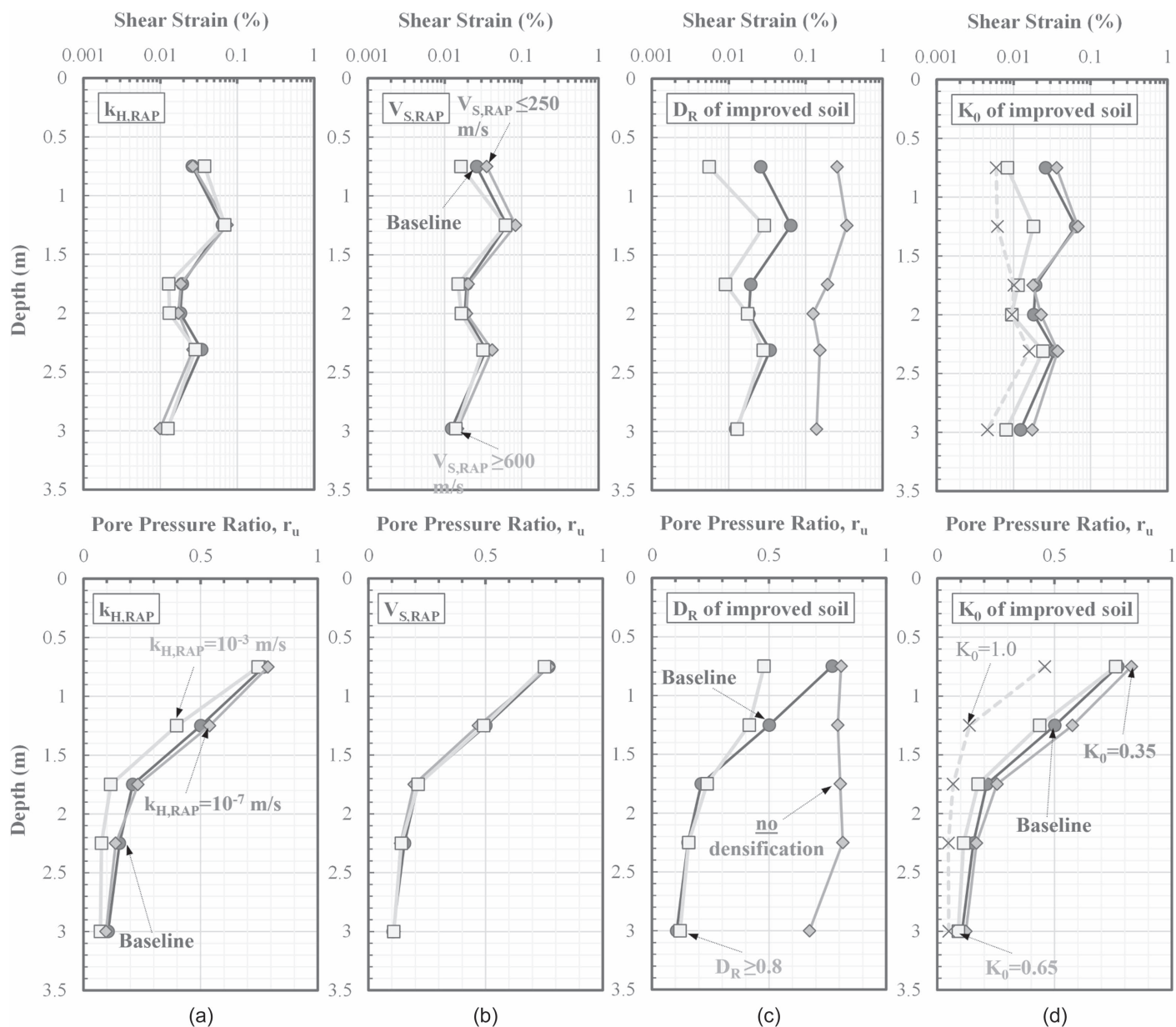


Fig. 20. Effect of (a) pier permeability ($k_{H,RAP}$); (b) pier shear stiffness ($V_{S,RAP}$); (c) relative density (D_R) of improved soil; and (d) lateral earth pressures (K_0) of improved soil on shear strains and excess pore pressure ratio r_u along the centerline of the PLAXIS3D model for earthquake bottom-up bidirectional shaking.

improved area and may not necessarily reflect the deformational response (e.g., settlements) of a potential foundation system at the improved ground surface.

Summary and Conclusions

A 3D numerical framework that leveraged full-scale testing of a stone column technique known as the rammed aggregate pier system is presented with the goal of assessing its performance in liquefiable soils, as well as understanding the contribution of different improvement mechanisms (such as drainage through the piers, densification of liquefiable soils, and pier inclusions) on the observed dynamic response. The analyses leveraged a large-scale ground improvement testing study that was conducted in Christchurch, New Zealand, following the 2010–2011 Canterbury Earthquake Sequence, which resulted in extensive infrastructure damage

caused by extreme levels of liquefaction-induced deformations. Specifically, the extensive in-situ site characterization, as well as full-scale testing using a vibroseis of three sites improved with the rammed aggregate pier system conducted by Roberts (2017), was considered. Informed by full-scale field testing observations, material parameter calibration results from 2D finite-difference simulations conducted by Thum et al. (2021), and strong earthquake ground motions recorded at a seismic station situated at a short distance from Site 6, a full 3D numerical assessment of the dynamic response of the natural and improved ground was performed in this study. Both natural and improved soil profiles were considered, and an advanced constitutive framework (UBCSand) was used to simulate the 3D cyclic behavior of liquefiable strata. The developed 3D models (Fig. 4) were subjected to top-down shaking, simulating the dynamic excitation exerted from the T-Rex vibroseis truck, as well as unidirectional and bidirectional

bottom-up shaking, recreating an earthquake scenario from the CES events. The PLAXIS 3D estimates resulting from simulations of T-Rex (top-down shaking at three different dynamic loads 1.5, 5, and 15 kPa) were shown to be in good agreement with the in-situ dynamic experiments both in terms of shear strain distributions with depth and excess pore pressure generation (Figs. 14 and 15).

Based on the 3D simulations that were validated against the field observations, the following conclusions were drawn:

1. Improved soil profiles experience reduced excess pore pressures (Figs. 13, 16, and 17) and dynamically induced shear strains (Figs. 11 and 18) compared to the natural, unreinforced soil cases. The developed 3D finite-element predictions were validated vis-à-vis the field observations.
2. Significant differences were observed between 2D and 3D simulations in calculated pore pressures for the T-Rex shaking at distances away from the T-Rex (Fig. 12). However, no field measurements are available in these areas.
3. Multidirectional shaking was found to have a significant effect on liquefaction triggering, particularly for the natural soil profiles, that is, bidirectional earthquake shaking results in substantially more extensive liquefied zones throughout the natural soil model compared to the unidirectional shaking scenario (Fig. 16). For the modeled geometry, the 3D pore pressures and shear strains along the centerline of the ground improvement can be sufficiently modeled in a plane strain 2D space [Fig. 18(b)] by using as input an earthquake record scaled by a factor of 1.11 to indirectly account for the influence of multidirectional shaking on liquefaction triggering.

In terms of mechanisms of improvement, the study shows that (1) soil densification around the pier elements contributed significantly to the reduction of the dynamically induced shear deformations and excess pore pressure generation during earthquake shaking [Fig. 20(c)], whereas (2) the increase in lateral earth pressures within the densified soil also resulted in a reduced deformational response [Fig. 20(d)]. Contrarily, the permeability and shear stiffness of the piers [Figs. 20(a and b)] did not have a significant influence on the pore pressure response, and shear strains developed along the centerline of the improved area.

The study highlights how the 3D numerical modeling of full-scale field experiments can generate insights on the response of a ground improvement scheme. From that perspective, the numerical methodology and calibration approach presented herein is appropriate for similar ground improvement schemes (e.g., stone columns). However, the parameter values derived from this work are representative of the specific construction technique used (e.g., RAP), type of full-scale testing conducted, and conditions encountered at the Christchurch site. More work needs to be conducted to better understand the contributing mechanisms for different stone column construction methods as well as a wider range of site conditions.

Data Availability Statement

Some data that support the findings of this study are available from the authors upon reasonable request.

Acknowledgments

Funding for this research was provided by Geopier Foundation Company. Any opinions, findings, and conclusions or recommendations expressed in this material are those of the authors and do not necessarily reflect the views of Geopier Foundation Company.

References

- Ashford, S. A., K. M. Rollins, and J. D. Lane. 2004. "Blast-induced liquefaction for full-scale foundation testing." *J. Geotech. Geoenviron. Eng.* 130 (8): 798–806. [https://doi.org/10.1061/\(ASCE\)1090-0241\(2004\)130:8\(798\)](https://doi.org/10.1061/(ASCE)1090-0241(2004)130:8(798)).
- Beatty, M. H., and P. M. Byrne. 2011. "UBCSAND constitutive model version 904aR." Accessed March 10, 2021. <https://www.itascacsg.com/software/udm-library/ubcsand>.
- Boulanger, R. W., and K. Ziotopoulou. 2018. *PM4Sand (Version 3.1): A sand plasticity model for earthquake engineering applications*. Rep. No. UCD/CGM-17/01. Davis, CA: Univ. of California.
- Cubrinovski, M., R. A. Green, and L. Wotherspoon. 2011. *Geotechnical reconnaissance of the 2011 Christchurch, New Zealand earthquake*. Berkeley, CA: Geotechnical Extreme Events Reconnaissance Association.
- Dimitriadi, V., G. Bouckovalas, Y. Chaloulos, and A. Aggelis. 2017. "Seismic liquefaction performance of strip foundations: Effect of ground improvement dimensions." *Soil Dyn. Earthquake Eng.* 106 (8): 298–307. <https://doi.org/10.1016/j.soildyn.2017.08.021>.
- Galavi, V., A. Petalas, and R. B. J. Brinkgreve. 2013. "Finite element modeling of seismic liquefaction in soils." *Geotech. Eng. J. SEAGS & AGSSEA* 44 (3): 55–64.
- Green, R. A., and J. Lee. 2012. "Liquefaction 560 risk mitigation." In *Deep foundations*. Hawthorne, NJ: The Magazine for the Deep Foundations Institute.
- Green, R. A., B. W. Maurer, and S. van Ballegooy. 2018. "The influence of the non-liquefied crust on the severity of surficial liquefaction manifestations: Case history from the 2016 Valentine's Day earthquake in New Zealand." In *Proc., Geotechnical Earthquake Engineering and Soil Dynamics V (GEESD V)*, Geotechnical Special Publication 290, edited by S. J. Brandenberg and M. T. Manzari, 21–32. Reston, VA: ASCE.
- Green, R. A., C. G. Olgun, and K. J. Wissmann. 2008. "Shear stress redistribution as a mechanism to mitigate the risk of liquefaction." In *Proc., Geotechnical Earthquake Engineering And Soil Dynamics*, Geotechnical Special Publication 181, edited by D. Zeng, M. T. Manzari, and D. R. Hiltunen, 1–10. Reston, VA: ASCE.
- Hutabarat, D., and J. D. Bray. 2021. "Effective stress analysis of liquefiable sites to estimate the severity of sediment ejecta." *J. Geotech. Geoenviron. Eng.* 147 (5): 04021024. [https://doi.org/10.1061/\(ASCE\)GT.1943-5606.0002503](https://doi.org/10.1061/(ASCE)GT.1943-5606.0002503).
- Idriss, I. M., and R. W. Boulanger. 2008. *Soil liquefaction during earthquakes*. Oakland, CA: Earthquake Engineering Research Institute.
- Ishihara, K. 1985. "Stability of natural deposits during earthquakes." In *Proc., 11th Int. Conf. on Soil Mechanics and Foundation Engineering*. Rotterdam, Netherlands: A. A. Balkema.
- Itasca. 2016. *FLAC—Fast Lagrangian analysis of continua, Version 8.0*. Minneapolis: Itasca Consulting Group.
- Kammerer, A., J. Wu, M. Riemer, J. Pestana, and R. Seed. 2004. "Shear strain development in liquefiable soil under bi-directional loading conditions." In *Proc., 13th World Conf. on Earthquake Engineering*. Vancouver, BC, Canada: 13 WCEE Secretariat.
- Kottke, A., and E. Rathje. 2008. *Technical manual for STRATA*. Rep. No. 2008/10. Berkeley, CA: Pacific Earthquake Engineering Research.
- Pyke, R., B. Seed, and C. Chan. 1975. "Settlement of sand under multidirectional shaking." *J. Geotech. J. Div.* 101 (4): 379–398. <https://doi.org/10.1061/AJGEB6.0000162>.
- Rathje, E. M., W. J. Chang, and K. H. Stokoe. 2005. "Development of an in situ dynamic liquefaction test." *Geotech. Test. J.* 28 (1): 50–60.
- Roberts, J. N. 2017. "Field evaluation of large-scale, shallow ground improvements to mitigate liquefaction triggering." Ph.D. thesis, Dept. of Civil, Architectural and Environmental Engineering, Univ. of Texas at Austin.
- Saftner, D. A., J. Zheng, R. A. Green, R. Hryciw, and K. Wissman. 2018. "Rammed aggregate pier installation effect on soil properties." *Proc. Inst. Civ. Eng.* 171 (2): 63–73. <https://doi.org/10.1680/jgrim.16.00021>.

- Seed, H. B., I. M. Idriss, F. Makdisi, and N. Banerjee. 1975. *Representation of irregular stress time histories by equivalent uniform stress series in liquefaction analysis*. Rep. No. EERC 75-2. Berkeley, CA: Earthquake Engineering Research Center.
- Seed, R. B., et al., 2003. "Recent advances in soil liquefaction engineering: A unified and consistent framework." In *Proc., 26th Annual ASCE Los Angeles Geotechnical Spring Seminar*. Berkeley, CA: Earthquake Engineering Research Center.
- Thum, T. S., A. Yerro, A. Saade, E. Ye, K. Wissmann, and R. A. Green. 2021. "Numerical modeling of rammed aggregate piers (RAP) in liquefiable soil." *Soil Dyn. Earthquake Eng.* 153 (Feb): 107088. <https://doi.org/10.1016/j.soildyn.2021.107088>.
- Tiznado, J. C., S. Dashti, C. Ledezma, B. P. Wham, and M. Badanagki. 2020. "Performance of embankments on liquefiable soils improved with dense granular columns: Observations from case histories and centrifuge experiments." *J. Geotech. Geoenviron. Eng.* 146 (9): 04020073. [https://doi.org/10.1061/\(ASCE\)GT.1943-5606.0002309](https://doi.org/10.1061/(ASCE)GT.1943-5606.0002309).
- van Ballegooy, S., J. Roberts, K. Stokoe, B. Cox, F. Wentz, and S. Hwang. 2015. "Large-scale testing of shallow ground improvements using controlled stage-loading with T-Rex." In *Proc., 6th Int. Conf. on Earthquake Geotechnical Engineering*. London: International Society of Soil Mechanics and Geotechnical Engineering.
- van Ballegooy, S., F. Wentz, K. Stokoe, B. Cox, K. Rollins, S. Ashford, and M. Olsen. 2017. *Christchurch ground improvement trial report*. Auckland, NZ: Tonkin & Taylor.
- White, D. J., H. T. Pham, and K. K. Hoevelkamp. 2007. "Support mechanisms of rammed aggregate piers. I: Experimental results." *J. Geotech. Geoenviron. Eng.* 133 (12): 1503–1512. [https://doi.org/10.1061/\(ASCE\)1090-0241\(2007\)133:12\(1503\)](https://doi.org/10.1061/(ASCE)1090-0241(2007)133:12(1503)).
- White, D. J., M. T. Sulieman, H. T. Pham, and J. Bigelow. 2002. *Constitutive equations for aggregates used in geopier foundation construction*. Ames, IA: Iowa State Univ.
- Wissmann, K. J., S. van Ballegooy, B. C. Metcalfe, J. Dismuke, and C. Anderson. 2015. "Rammed aggregate pier ground improvement as a liquefaction mitigation method in sandy and silty soils." In *Proc., 6th Int. Conf. on Earthquake Geotechnical Engineering*. London: International Society of Soil Mechanics and Geotechnical Engineering.